
National Laser Users' Facility and External Users' Programs

During FY08, a governance plan was implemented to formalize the scheduling of the OMEGA Laser Facility as an NNSA User Facility. Under this plan, OMEGA shots are allocated by campaign. The majority of the FY08 target shots were allocated to the National Ignition Campaign (NIC), and integrated experimental teams from LLNL, LANL, SNL, and LLE conducted a variety of NIC-related experiments primarily at the OMEGA Laser Facility. Shots were also allocated in FY08 to the high-energy-density (HED) physics programs from LLNL and LANL.

Under the governance plan, 25% of the facility shots are allocated to Basic Science experiments. Roughly half of these are dedicated to University Basic Science under the National Laser Users' Facility program, and the remaining shots are allotted to Laboratory Basic Science, comprising peer-reviewed basic science experiments conducted by the national laboratories and LLE/FSC.

The OMEGA Facility is also being used for several campaigns by teams from the Commissariat à l'Énergie Atomique (CEA) of France and AWE of the United Kingdom. These programs are conducted at the facility on the basis of special agreements put in place by DOE/NNSA and the participating institutions.

The external users during this year included six collaborative teams participating in the National Laser Users' Facility (NLUF) program; many collaborative teams from the national laboratories conducting experiments for the National Ignition Campaign (NIC); investigators from LLNL and LANL conducting experiments for HED physics programs; and scientists and engineers from CEA of France and AWE of the United Kingdom.

In this section, we briefly review all the external user activity on OMEGA during FY08, including NLUF programs and experiments conducted by users from LLNL, LANL, CEA, and AWE.

NLUF Program

In FY08, the Department of Energy (DOE) issued a solicitation for NLUF grants for the period of FY09–FY10.

A total of 13 proposals were submitted to DOE for the NLUF FY09–FY10 program. An independent DOE Technical Evaluation Panel comprised of Dr. Steven Batha (LANL), Dr. Gilbert (Rip) Collins (LLNL), Dr. Ramon Leeper (SNL), Prof. Howard Milchberg (University of Maryland), and Prof. Donald Umstadter (University of Nebraska, Lincoln) reviewed the proposals on 18 April 2006 and recommended that 11 of the proposals receive DOE funding and shot time on OMEGA in FY09–FY10. Table 116 IV lists the successful proposals.

FY08 NLUF Experiments

FY08 was the second of a two-year period of performance for the NLUF projects approved for the FY07–FY08 funding and OMEGA shots. Six of these NLUF projects were allotted OMEGA shot time and received a total of 125 shots on OMEGA in FY08. Some of this work is summarized in this section.

Experimental Astrophysics on the OMEGA Laser

Principal Investigator: R. P. Drake (University of Michigan)
Co-investigators: D. Arnett (University of Arizona); T. Plewa (Florida State University); A. Calder (University of Chicago); J. Glimm, Y. Zhang, and D. Swesty (State University of New York–Stony Brook); M. Koenig (LULI, École Polytechnique, France); C. Michaut (Observatoire de Paris, France); M. Busquet (France); J. P. Knauer and T. R. Boehly (LLE); P. Ricker (University of Illinois); and B. A. Remington, H. F. Robey, J. F. Hansen, A. R. Miles, R. F. Heeter, D. H. Froula, M. J. Edwards, and S. H. Glenzer (LLNL)

The OMEGA laser, with its ability to produce pressures greater than 10 Mbars, can create conditions of very high energy density that are relevant to astrophysical phenomena. This project explores two such issues: the contribution of hydrodynamic instabilities to the structure in supernovae and the dynamics of radiative shock waves. The study of radiative shock dynamics is a continuation of successful campaigns at LLE that have employed x-ray radiography to quantify the average shock velocity and the structure of the dense, shocked matter. Of primary importance to understanding the role played

Table 116.IV: FY09–FY10 NLUF Proposals.

Principal Investigator	Affiliation	Proposal Title
F. Beg	University of California, San Diego	Systematic Study of Fast Electron Transport and Magnetic Collimation in Hot Plasmas
R. P. Drake	University of Michigan	Experimental Astrophysics on the OMEGA Laser
R. Falcone	University of California, Berkeley	Detailed <i>In-Situ</i> Diagnostics of Multiple Shocks
U. Feldman	ARTEP, Inc.	EP-Generated X-Ray Source for High Resolution 100–200 keV Point Projection Radiography
Y. Gupta	Washington State University	Ramp Compression Experiments for Measuring Structural Phase Transformation Kinetics on OMEGA
P. Hartigan	Rice University	Dynamics of Shock Waves in Clumpy Media
R. Jeanloz	University of California, Berkeley	Recreating Planetary Core Conditions on OMEGA, Techniques to Produce Dense States of Matter
K. Krushelnick	University of Michigan	Intense Laser Interactions with Low Density Plasmas Using OMEGA EP
R. Mancini	University of Nevada, Reno	Three-Dimensional Studies of Low-Adiabatic Direct-Drive Implosions at OMEGA
M. Meyers	University of California, San Diego	Response of BCC Metals to Ultrahigh Strain Rate Compression
R. D. Petrasso	Massachusetts Institute of Technology	Monoenergetic Proton and Alpha Radiography of Laser-Plasma-Generated Fields and of ICF Implosions

by radiation in the shock dynamics is the electron temperature throughout the shocked material. We have used x-ray Thomson scattering to make such temperature measurements.

In the experiment, ten OMEGA laser beams irradiate a Be drive disk with UV light for 1 ns. The beams deposit a total energy of ~ 3.8 KJ, giving an average irradiance of $\sim 4.8 \times 10^{14}$ W/cm², corresponding to an ablation pressure of ~ 46 Mbar in the Be drive disk. The enormous pressure first launches shocks and then accelerates the Be material, which in turn drives a shock into a cylinder filled with Ar gas. The shock moves through the Ar with an average velocity of the order of ~ 150 km/s, which is fast enough that radiative effects play a significant role in the shock dynamics. An additional eight OMEGA laser beams irradiate a Mn foil for 1 ns to create the x rays needed to probe the shocked Ar system. The x rays are scattered through an average angle of 100° before being spectrally resolved by a crystal spectrometer and then detected by a four-strip gated microchannel plate.

Figure 116.55 shows some of the resulting data. The probe for these data was offset from the drive beams by 15 ns, placing the measurement in the precursor region of the shock. Additional measurements were made at different times, cor-

responding to different regions in the shock system. The signal includes two peaks produced by elastic scattering from tightly bound electrons and a broad red-shifted feature expected from

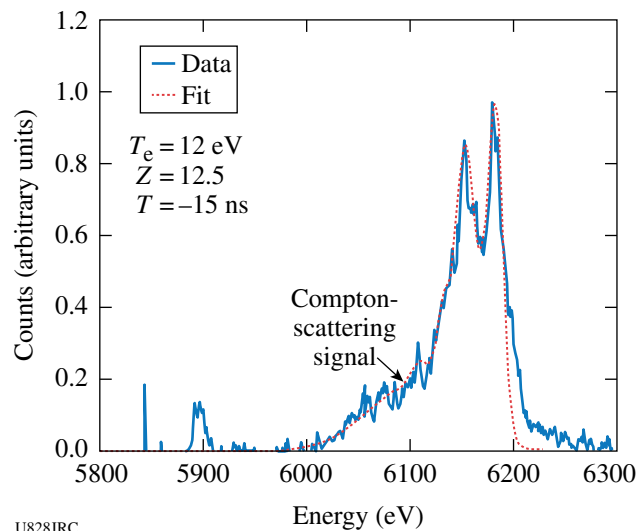


Figure 116.55 Spectrum of x-ray Thomson-scattered light from the precursor region of radiative shock, showing peaks from elastic scattering and a shifted feature from free electrons.

photons that are Compton scattered from the free electrons. By fitting a theoretical line to the observed signal, the electron temperature and average ionization can in principle be deduced. The fit shown is preliminary.

Laboratory Experiments of Supersonic Astrophysical Flows Interacting with Clumpy Environments

Principal Investigator: P. Hartigan (Rice University)
 Co-investigators: R. Carver and J. Palmer (Rice University); J. Foster, P. Rosen, and R. Williams (AWE); B. Wilde and M. Douglas (LANL); A. Frank (University of Rochester); and B. Blue (General Atomics)

Strong shock waves occur in many astrophysical systems, and the morphology of the emission lines that occur from the hot gas behind these shocks is often highly clumpy. The objective of this sequence of NLUF experiments is to develop scaled laboratory experiments to study the hydrodynamics of clumpy supersonic flows. The laboratory work complements new astrophysical images from the Hubble Space Telescope (HST) that were motivated by the results of the NLUF program.

Our work in the past year has concentrated first on developing and implementing an experimental design that could follow the destruction of a single clump by the passage of a strong shock and then expanding this work to include two clumps that are close enough that shadowing significantly affects the dynamics of the interactions. A sample of the results from these successful experiments appears in Fig. 116.56. Upper panels (a) and (b) show how a single clump flattens and the bow shock widens as time progresses in the interaction. Remarkably, we have now seen this exact phenomenon in our most-recent image of one of the knots in a Herbig–Harro object (HH 2). The bottom panels show H α images obtained with HST in 1994, 1997, and 2007. The new bow shock clearly expands as a result of the strong wind that passes from right to left in the figure.

A large complex region of multiple clumps within HH 2 shown in the figure appears to have significant morphological changes. In several cases significant differential motions exist between adjacent clumps, and it now appears that shadowing and merging are probably common in such flows. We see

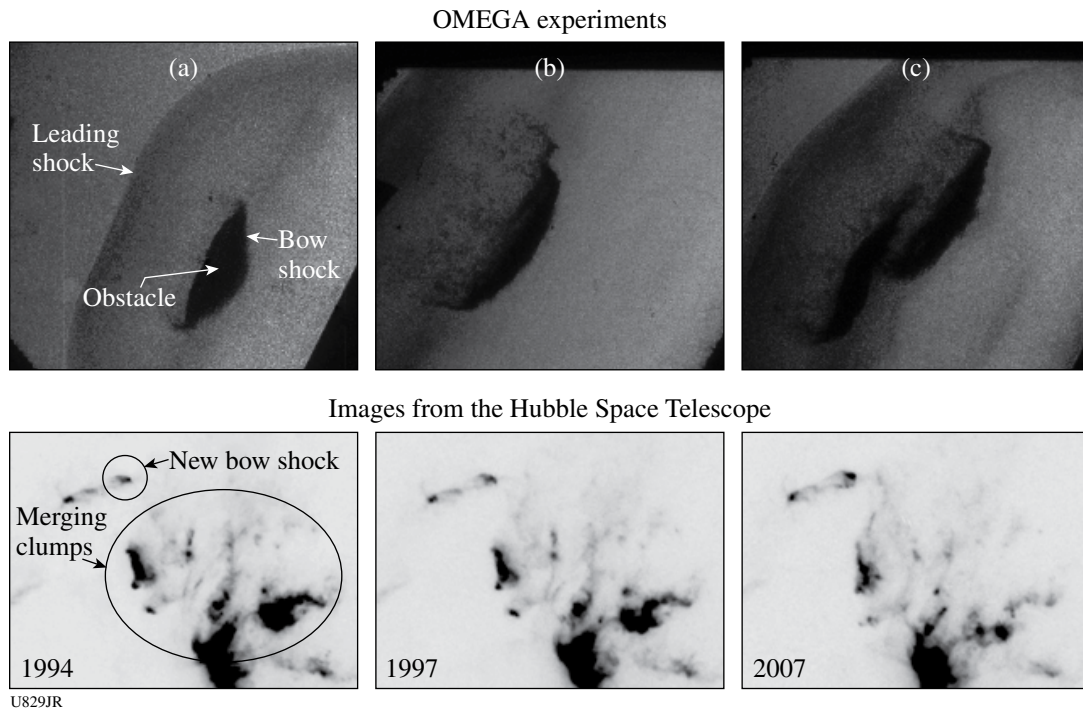


Figure 116.56 OMEGA experiments (top) and three astronomical images (bottom) of shock waves around single and multiple clumps. The experimental images (a) and (b) show how a shock wave flattens and tears apart an obstacle. Analogous behavior has just been observed unambiguously for the first time with a third-epoch Hubble Space Telescope image of shocks in HH 2 (bottom). Note how the new bow shock widens in the most-recent 2007 image. The third experimental image (c) shows how shadowing affects two clumps. Multiple clump interactions also occur in HH 2.

analogous behavior in the laboratory experiment labeled (c) where shadowing effects have created a bumpy bow shock around two closely spaced obstacles in the flow. In the coming year we will be evolving this design to address shocked flow through a medium with dozens of small clumps. Two additional third-epoch HST images will complement the experimental work in the coming year.

Multiview Tomographic Study of OMEGA Direct-Drive Implosion Experiments

Principal Investigators: R. Mancini (University of Nevada, Reno), R. Tommasini (LLNL)

Co-investigators: N. Izumi (LLNL); I. E. Golovkin, (Prism Computational Sciences); D. A. Haynes and G. A. Kyrala (LANL); and J. A. Delettrez, S. P. Regan, and V. A. Smalyuk (LLE)

The determination of the spatial structure of inertial confinement fusion implosion cores is an important problem of high-energy-density physics. To this end, three identical multimonoenergetic x-ray imagers (DDMMI's), designed and built as part of this project, are currently being used in direct-drive OMEGA implosion experiments to perform simultaneous observations along three quasi-orthogonal lines of sight (LOS). The implosions are driven with 60 OMEGA beams using high- and low-adiabat laser pulses, and the targets are gas-filled plastic shells. At the collapse of the implosion, the hot and dense core plasma achieves temperatures in the 1-keV to 2-keV range and electron number densities in the $1 \times 10^{24} \text{ cm}^{-3}$ to $3 \times 10^{24} \text{ cm}^{-3}$ range. X-ray K-shell line emission from a tracer amount of argon added to the deuterium fuel is a suitable spectroscopy diagnostic for this temperature and density range. In addition, x-ray absorption from a titanium tracer layer embedded in the plastic yields information about the compressed shell.

Core images recorded by DDMMI instruments are formed by a large array of $10\text{-}\mu\text{m}$ -diam pinholes, with an $\sim 100\text{-}\mu\text{m}$ separation between pinholes, and are reflected off a depth-graded WB_4C multilayer mirror with an average bilayer thickness of 15 \AA . The instrument is equipped with 10-cm-long mirrors that permit the observation of narrowband x-ray images over a 3-keV to 5-keV photon energy range. They have a magnification of 8.5, provide spatial resolution of approximately $10 \mu\text{m}$, and record gated (framed) images characteristic of a 50-ps time interval. The broad photon energy range, afforded by the use of long mirrors, covers the K-shell line emission from argon ions as well as the K-shell line absorption from titanium L-shell ions. As an illustration

of the data recorded by DDMMI instruments, Fig. 116.57 displays gated argon $\text{Ly}\beta$ ($1s^2S-3p^2P$, $h\nu = 3936 \text{ eV}$) narrowband core images observed simultaneously along three quasi-orthogonal LOS: TIM-3, TIM-4, and TIM-5. These images are taken close to the state of maximum compression of the core. The photon energy range of these narrowband images is given by the (mainly) Stark-broadening widths of the line shape, which for the plasma conditions achieved in these cores is in the 60-eV to 70-eV range. The multiview data recorded with DDMMI instruments make it possible to study the three-dimensional structure of the implosion core. It is interesting to observe the differences in distribution of brightness associated with the $\text{Ly}\beta$ core images along different LOS, which depends on both temperature and density conditions in the core. In addition to differences in intensity distributions, there are differences in shapes: the image observed along TIM-4 is the most-elongated one (i.e., oval of largest eccentricity), while the shapes observed along TIM-3 and TIM-5 are less elongated. Argon $\text{Ly}\alpha$ ($1s^2S-2p^2P$, $h\nu = 3320 \text{ eV}$) and $\text{He}\beta$ ($1s^2^1S-1s3p^1P$, $h\nu = 3684 \text{ eV}$) images are also recorded, thus providing data that will determine the temperature and density distribution in the core. Several analysis methods initially developed and tested for single LOS data analysis are now being extended to consider the analysis of data simultaneously observed along three LOS for a three-dimensional reconstruction of the spatial structure in the core.

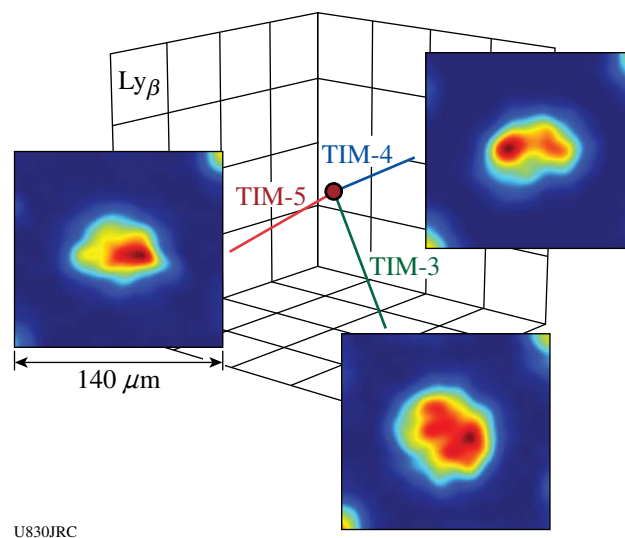


Figure 116.57
Gated argon $\text{Ly}\beta$ narrowband images of the implosion core simultaneously recorded by DDMMI instruments along three quasi-orthogonal lines of sight: TIM-3, TIM-4, and TIM-5 for OMEGA shot 49956.

Monoenergetic Proton Radiography of ICF Implosions

Principal Investigators: R. D. Petrasso and C. K. Li (Massachusetts Institute of Technology)

Co-investigators: F. H. Séguin and J. A. Frenje (MIT); J. P. Knauer and V. A. Smalyuk (LLE); and J. R. Rygg and R. P. J. Town (LLNL)

MIT's NLUF program has continued an ongoing series of experiments using monoenergetic charged-particle radiography in the study of plasmas and transient electromagnetic fields generated by the interactions of OMEGA laser beams with plastic foils and ICF target capsules. This work, involving novel studies of field instabilities, magnetic reconnection, ICF implosion dynamics, and self-generated electromagnetic fields in ICF implosions, has already resulted in many publications, including four in *Physical Review Letters*¹⁻⁴ and one in *Science*,⁵ as well as several invited talks at conferences.⁶⁻⁹

Figure 116.58 shows the basic experimental setup for imaging of implosions (see Ref. 10 for more general details of the radiography method). Up to 40 OMEGA laser beams interact with a target capsule, which has a spherical plastic shell with or without a gold cone inserted for "fast-ignition" studies. A radiographic image of the imploded capsule is made by using a special backlighter and a matched imaging detector. The backlighter is a glass-shell ICF capsule filled with D³He gas and imploded by ~20 OMEGA laser beams, producing D³He protons (14.7 MeV) and other fusion products. CR-39 nuclear track detectors are used in conjunction with appropriate filters and processing techniques to record individual charged particles and their energies in the detector plane. Since the burn duration of the D³He implosion is short (~130 ps) relative to the nanosecond-scale duration of the capsule illumination (1 ns) and subsequent evolution, and since the relative timing of the backlighter and

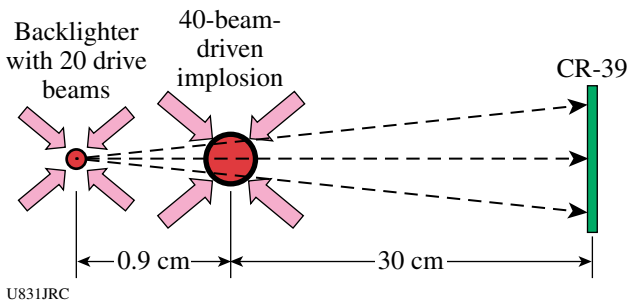


Figure 116.58 Experimental setup with proton backlighter, subject implosion, CR-39 imaging detector, and laser beams. The subject implosion shown here has a spherical plastic shell, but images were also made with "cone-in-shell" capsules (see Fig. 116.59).

the capsule illumination was adjustable, it is possible to record images at different times during implosions.

The experiments resulted in the discovery and characterization of two distinctly different types of electromagnetic configurations in ICF implosions (Fig. 116.59), as well as the measurement of capsule radius and areal-density (ρR) temporal evolution (Fig. 116.60).^{4,5} Proton radiography reveals field structures through deflection of proton trajectories. The two field structures evident in Fig. 116.59 consist of (1) many radial filaments with complex striations and bifurcations, permeating the entire field of view, of magnetic field magnitude 60 T; and (2) a coherent, centrally directed electric field of the order of 10^9 V/m within the capsule, leading to the central concentration of protons in Fig. 116.59(b). Figure 116.60 shows the values of capsule radius and ρR at various times during the implosions of spherical capsules studied in images similar to those in Fig. 116.59.⁴ The size was inferred from the spatial structure of the images, while ρR was determined from the energy loss of the imaging protons while passing through the capsule center.

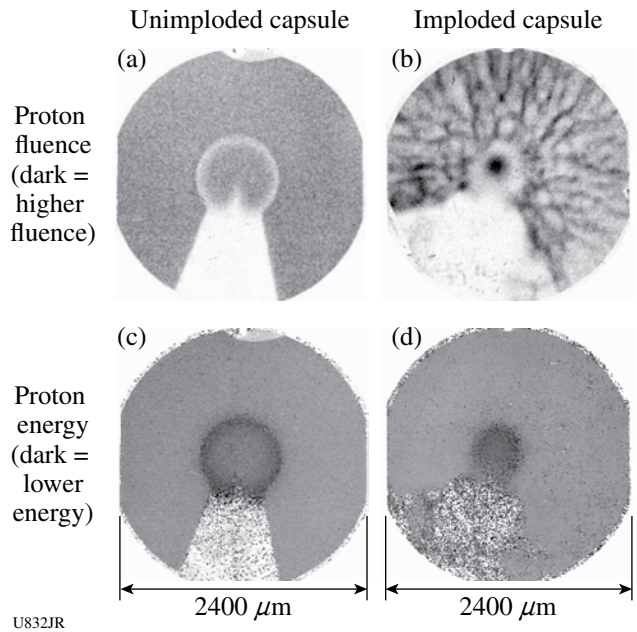
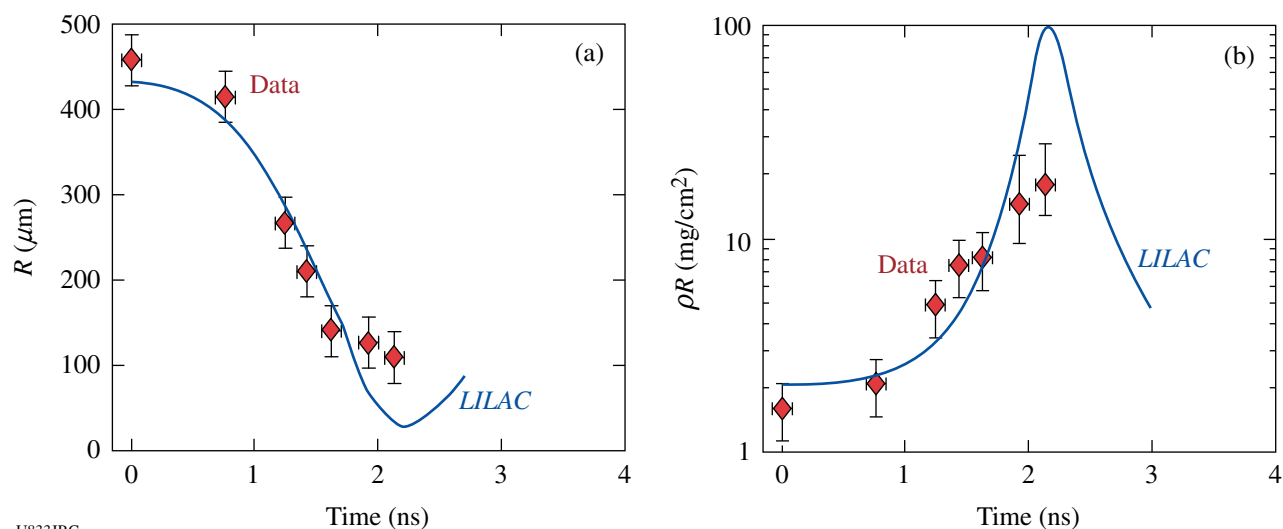


Figure 116.59 Images of a 430- μm -radius spherical CH capsule with attached gold cone, before and during implosion. Images (a) and (c) show the unimploded capsule used in OMEGA shot 46531. Images (b) and (d) show a capsule at 1.56 ns after the onset of the laser drive (shot 46529). In (a) and (b) dark areas correspond to regions of higher proton fluence, while in (c) and (d) dark areas correspond to regions of lower proton energy. The energy image values in the region shadowed by the cone are mostly noise since very few protons were detected in that region.



U833JRC

Figure 116.60

Measured capsule radius (a) and ρR (b) as a function of time,⁴ from a series of images of spherical implosions (40 drive beams in a 1-ns flat-top pulse). The curves show *LILAC* 1-D simulations.

The relationship of the measured sizes and ρR 's to predictions of the 1-D code *LILAC* are also shown.

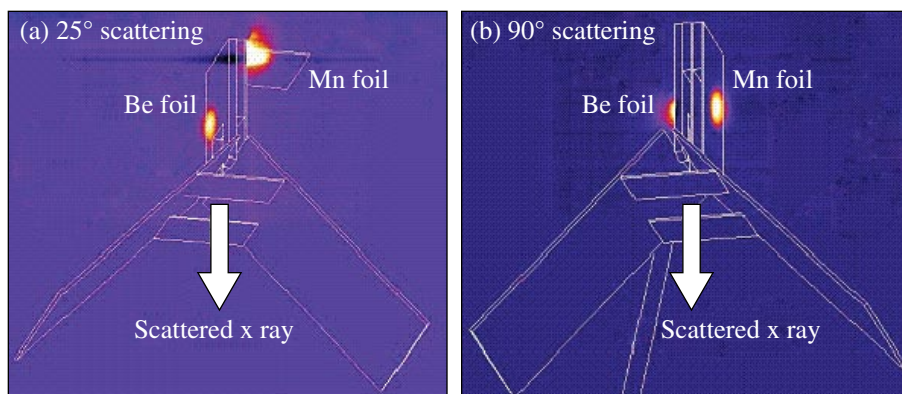
X-Ray Thomson-Scattering Spectra in Shock-Compressed Beryllium

Principal Investigators: R. Falcone and H. J. Lee (University of California, Berkeley), P. Neumayer and S. H. Glenzer (LLNL)

Direct measurement of the exact thermodynamic and physical properties of dense matter is of great interest to test dense plasma modeling and to address fundamental physics questions such as the equation of state and the structure of dense matter. Powerful laser-produced x-ray sources have been used to probe dense matter, which has enabled a quantitative *in-situ* diagnostic of densities and temperatures using x-ray Thomson scattering measurements.¹¹ We have continued x-ray scattering experi-

ments in shock-compressed beryllium to measure the electron temperature and density for varying drive-beam conditions.

Two types of planar targets coupled with Mn backlighters were deployed for the x-ray Thomson-scattering measurements of 25° and 90° scattering angles on the OMEGA laser. A 250- μm -thick beryllium foil was driven by 12 beams smoothed with distributed phase plates (SG-4) overlapped in a $\sim 1\text{-mm}$ -diam focal spot. Laser intensities of $10^{14} \text{ W/cm}^2 < I < 10^{15} \text{ W/cm}^2$ in a 4-ns-long constant or 5-ns shaped pulse were applied. Radiation-hydrodynamic calculations performed using Helios¹² indicate that under these irradiation conditions, a strong shock wave is launched in the solid target, compressing it homogeneously at pressures in the range of 20 to 60 Mbar. Twelve additional focused beams ($\sim 200\text{-}\mu\text{m}$ spot) illuminate a Mn foil to produce $\sim 6.18\text{-keV}$ $\text{He}\alpha$ x rays for 25° scattering (17 backlighter beams are used for 90° scattering). Figures 116.61(a) and 116.61(b)



U861JRC

Figure 116.61

Time-integrated images for $E > 2 \text{ keV}$ show the emission produced by heater and probe beams for (a) 25° scattering and (b) 90° scattering.

present time-integrated images showing the emission by drive and backlighter beams. A highly oriented pyrolytic graphite (HOPG) crystal spectrometer coupled to a gated microchannel plate detector in TIM-3 has been used as a spectrometer and a detector. The scattered photon fraction is determined by the product $n_e \sigma_{\text{TSL}}$, where σ_{TSL} is the Thomson-scattering cross section and l is the length of the scattering volume.

Figures 116.62(a) and 116.62(b) show the scattering spectra (solid lines) and fits (dotted lines) for a 25° and a 90° scattering angle from 4-ns-long constant drive beams, which give a pressure of 30 Mbar. Two small plasmon features in addition to the two elastic peaks from the 6.18-keV Mn He $_{\alpha}$ line and the 6.15-keV intercombination line are measured at a 25° scattering angle, indicating a collective scattering regime with a scattering parameter $\alpha = 1/k\lambda_s = 1.56$ and λ_s being the screening length and k the scattering vector with

$k = 4\pi(E_0/hc) \sin g(\theta/2) = 1.36 \text{ \AA}^{-1}$. The frequency shift of the plasmon is determined by the frequency of plasma oscillations. Calculated spectra using the theoretical form factor indicate that the solid beryllium is compressed by a factor of 3 with $7 \times 10^{23} \text{ cm}^{-3} < n_e < 8 \times 10^{23} \text{ cm}^{-3}$.

The Compton-scattering spectrum measured at a scattering angle of $\theta = 90^\circ$ accessing the noncollective scattering regime with $\alpha = 0.5$ and $k = 4.4 \text{ \AA}^{-1}$ shows a parabolic spectrum downshifted in energy from the incident radiation by the Compton effect; the shift is determined by the Compton energy $E_C = \hbar^2 k^2 / 2m_e = 74 \text{ eV}$. The theoretical fit to the measured spectrum indicates the same densities and temperatures as obtained for collective scattering. Details may be found in Ref. 13.

To generate higher compression, the intensity of nanosecond laser beams was shaped to have (1) a 4-ns-long step-like foot,

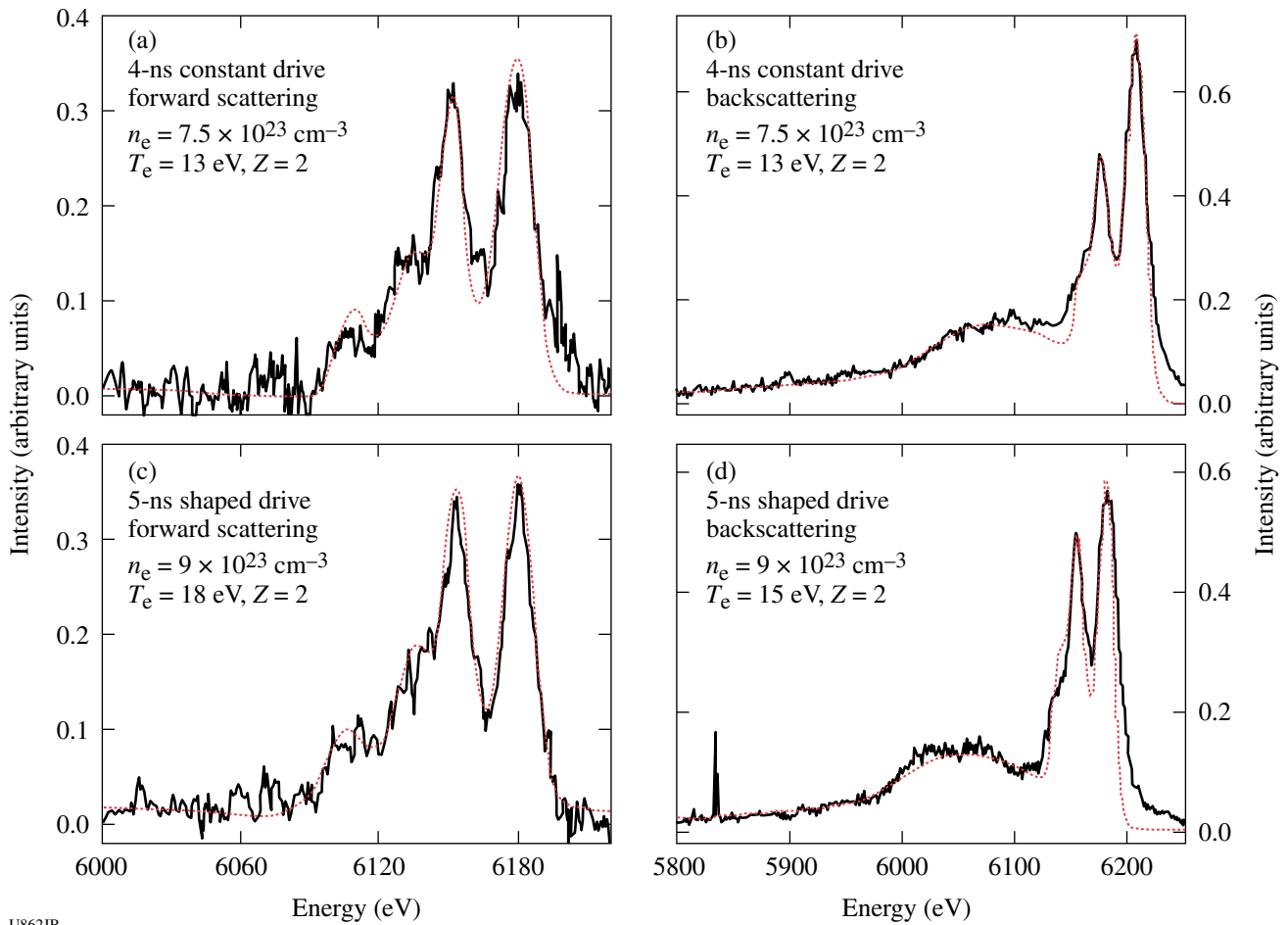


Figure 116.62

X-ray scattering data (solid lines) and fits (dotted lines) of 25° forward scattering [(a) and (c)] and 90° backscattering [(b) and (d)] with different driving beams.

with a 2-ns first foot at 8×10^{13} W/cm² and a 2-ns second foot at 1.6×10^{14} W/cm² and (2) a 1-ns-long peak at 4.8×10^{14} W/cm² following a 4-ns step-like foot. Radiation-hydrodynamic simulations show that the three shock waves from each step merge at about 6 ns after the beginning of drive beams and compress the target by more than a factor of 3.5.

Figures 116.62(c) and 116.62(d) show the experimental scattering spectra (solid lines) at a 25° and a 90° scattering angle and fits (dotted lines) from 5-ns-long shaped drive beams that drive a strong shock reaching ~60 Mbar. The calculated spectrum with $n_e = 9 \times 10^{23}$ cm⁻³, $T_e = 15$ eV, and $Z = 2$ gives a best fitting to the Compton-scattering data. The parameters from the fit to the data in the collective scattering regime are in good agreement with the ones from the noncollective scattering data within error bars of $\pm 20\%$ in temperature. Theoretical x-ray scattering spectra have been calculated in a random phase approximation for the free-electron feature and density-functional theory for the ion feature.

Through this campaign, we have successively accomplished the measurement of the Compton and plasmon resonance on shock-compressed Be. In addition to the accurate measurement within $\pm 7\%$ in density, we have demonstrated that we can characterize multiply shocked matter by changing the drive pulse shape and intensity. This opens up the possibility of obtaining a compression of $n_e > 1.0 \times 10^{24}$ cm⁻³ by co-propagating and counter-propagating the geometry of driving beams. In future research, the Thomson-scattering method will be used to investigate the equation of state in the multiple-shock-compressed matter.

FY08 LLNL OMEGA Experimental Programs

In FY08, Lawrence Livermore National Laboratory (LLNL) led 238 target shots on the OMEGA Laser System. Approximately half of these experiments were dedicated to the National Ignition Campaign (NIC); the other half were dedicated to supporting the high-energy-density stewardship experiments (HEDSE's).

Objectives of the LLNL-led NIC campaigns on OMEGA included the following:

- *Laser-plasma interaction studies of physical conditions relevant for the National Ignition Facility (NIF) ignition targets*
- *Studies of the x-ray flux originating from the laser entrance hole (LEH) window of a hohlraum, which might impact the performance of a fusion capsule*

- *Characterization of the properties of warm dense matter—specifically radiatively heated Be*
- *Studies of the physical properties of capsules based on Cu-doped Be, high-density carbon, and conventional plastics, including new high-resolution shock-velocity measurements*
- *Determining ablator performance during the implosion of NIC-candidate ablaters*
- *Experiments to study the physical properties (thermal conductivity) of shocked fusion fuels*
- *High-resolution measurements of velocity nonuniformities created by microscopic perturbations in NIF ablator materials*
- *Demonstration of $T_r = 100$ -eV foot-symmetry tuning using a re-emission sphere*
- *Demonstration of $T_r = 100$ -eV foot-symmetry tuning using a backlit thin-shell capsule*
- *Quantification of x-ray foot preheat caused by laser-window interaction*

The LLNL HEDSE campaigns included the following:

- *Quasi-isentropic [isentropic compression experiment (ICE)] drive used to study material properties such as strength, equation of state, phase, and phase-transition kinetics under high pressure*
- *Development of long-duration, point-apertured, point-projection x-ray backlighters*
- *Development of an experimental platform to study non-local thermodynamic equilibrium (NLTE) physics using direct-drive implosions*
- *Opacity studies of high-temperature plasmas under LTE conditions*
- *Development of multikilovolt x-ray sources using underdense NLTE plasmas for x-ray source applications*
- *Studies of improved hohlraum heating efficiency using cylindrical hohlraums with foam walls*

- Laser-driven dynamic-hohlraum (LDDH)-implosion experiments
- High-speed hydrodynamic jets for code validation

1. NIC Experiments

Laser-Plasma Interactions: The laser-plasma interaction experiments continued to emulate the plasma conditions expected along the laser-beam path in inertial confinement fusion designs. An interaction beam (beam 30) aligned along the axis of a gas-filled hohlraum is used to study laser-beam propagation. Figure 116.63 shows the results of laser-plasma interaction experiments that were performed to study the propagation of laser light through high-density ($N_e/N_{cr} > 10\%$), millimeter-long, high-temperature ($T_e > 2.5$ keV) plasmas. These results provide limits on the intensity of the inner-cone beams to maintain stimulated Raman scattering (SRS) backscatter below the 5% requirements for ignition on the NIF.

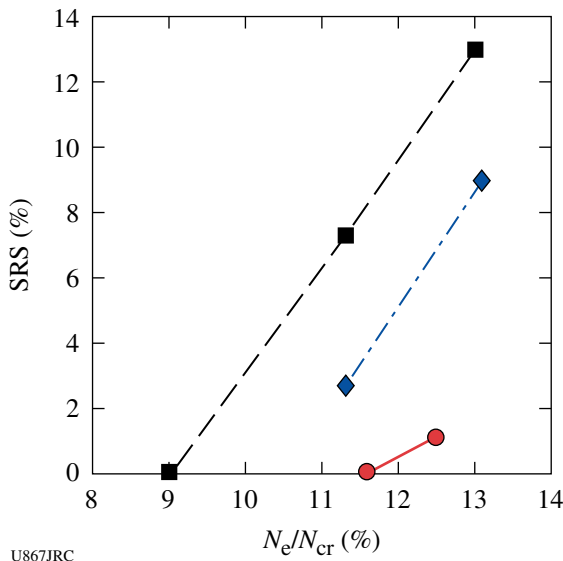


Figure 116.63 Measured time-integrated backscatter as a function of density in a high-temperature millimeter-long plasma at three interaction-beam intensities: 10×10^{14} W/cm² (squares), 5×10^{14} W/cm² (diamonds), and 2.5×10^{14} W/cm² (circles). For densities above 10%, the backscatter is dominated by stimulated Raman scattering (SRS); the measured time-integrated stimulated Brillouin scattering (SBS) is less than 1%.

These experiments also quantified the effect of polarization smoothing in high-density plasmas where SRS dominates, providing further guidance for the design of a low-backscatter, indirect-drive ICF experiment. Figure 116.64 shows that adding polarization smoothing increases the intensity threshold

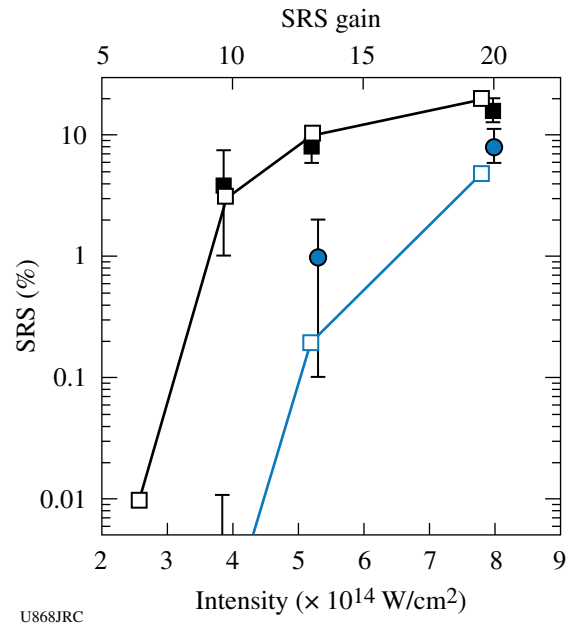


Figure 116.64 Instantaneous SRS reflectivities measured 700 ps after the rise of the heater beams in a 11.5% N_{cr} plasma. Experiments without polarization smoothing (squares) show a threshold (reflectivity of 5%) for SRS at an intensity of 4.5×10^{14} W/cm² and a corresponding gain of 11. Adding polarization smoothing increases this threshold to an intensity of 6.8×10^{14} W/cm², which corresponds to an SRS gain of 17. *pf3D* simulations performed prior to the experiments are shown (open symbols) and predicted the main results of these experiments. The gains are calculated by post-processing hydrodynamic simulations using *LIP*.

for SRS by a factor of 1.5, which was predicted by *pf3D* code simulations completed prior to these experiments.

Prior work on stimulated Brillouin scattering (SBS) mitigation was documented and published in Refs. 14 and 15.

X-Ray Preheat from an LEH Window: The NIF ignition hohlraum was gas filled with polyimide windows over the laser entrance holes. During the early part of the laser pulse, the beams had to burn through the windows and fill-gas before reaching the hohlraum walls. As a result, the x rays generated during window burnthrough occurred ~ 300 ps before the hohlraum x rays. There was concern that the resultant early deposition of energy at the capsule poles could have generated an asymmetric pressure wave, or that asymmetric preheat could have seeded instabilities in crystalline Be. Initial *LASNEX* calculations predicted that x-ray production would not be high enough to significantly perturb the capsule, but an extrapolation of existing experimental data suggested that *LASNEX* might have underestimated the flux from the windows. A short series of OMEGA shots were carried out to measure the absolute x-ray spectrum generated during burnthrough of polyimide windows of various thicknesses, and

the inner- to outer-beam cone delay and intensities spanning those expected to be used on the NIF. The primary diagnostic on these shots was the Dante x-ray diode array.

Figure 116.65 shows the measured flux from Channel 5 (centered from 600 to 800 eV) for a series of five shots, together with *LASNEX* simulations for each shot. The results showed that in all cases the measured flux integrated over the first nanosecond was $\sim 2\times$ lower than predicted by *LASNEX*. The x-ray flux scaled as expected—approximately linearly with window thickness.

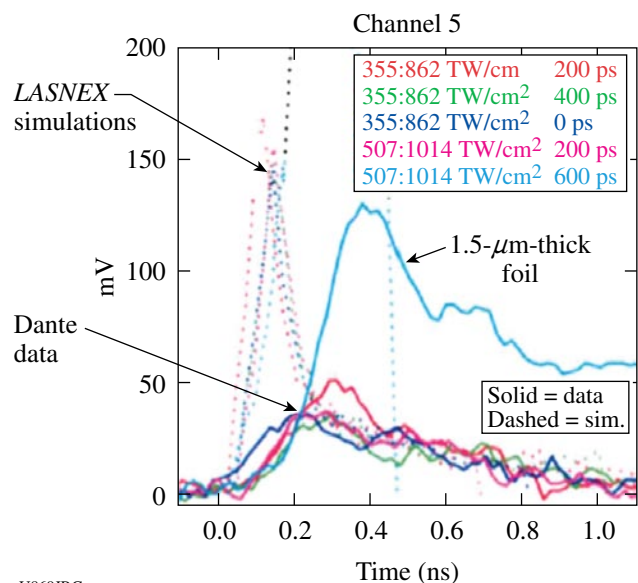


Figure 116.65
A measured signal from Dante Channel 5 for the window preheat shots. The legend shows an intensity of cone-1 beams in TW/cm^2 (first number), cone-2 intensity (second number), and the delay between beams (third number). The indicated curve depicts a $1.5\text{-}\mu\text{m}$ -thick foil; all others have $0.5\text{-}\mu\text{m}$ thickness.

Since no adverse effect was expected on the capsule even with nominal x-ray production, the low measured x-ray flux indicated that the ignition point design was robust to perturbations imposed on the capsule during window burnthrough.

Symmetry Diagnosis by a Re-emission Sphere: The NIC proposes to set the first 2 ns of hohlraum radiation symmetry by observing the instantaneous soft x-ray re-emission pattern from a high-Z sphere in place of the ignition capsule.¹⁶ To assess this technique under NIC conditions, we used the OMEGA Laser Facility to image the re-emission of Bi-coated spheres with 200-ps temporal, 50- to $100\text{-}\mu\text{m}$ spatial, and 30% spectral resolution. The sphere was driven by 70% NIC-scale vacuum Au hohlraums heated to $T_r = 100\text{ eV}$ using two cones/ side laser-beam illumination (Fig. 116.66). The laser beams smoothed with SG4 phase plates using 1-ns square pulses generated intensities at the hohlraum wall that were similar to the foot of the NIF ignition design.

Good re-emit images were acquired at 100- to 115-eV NIF foot temperatures for both 900- and 1200-eV energy bands (see Fig. 116.67). The re-emission patterns at 900 eV and 1200 eV were consistent with each other, but their sensitivity ratio was greater than expected; this will be confirmed in FY09. We also demonstrated the expected P_2/P_0 dependence to the laser-cone power ratio (Fig. 116.67). The experiments demonstrated the required accuracies of $<5(7\%) P_2/P_0$ (P_4/P_0) Legendre mode-flux asymmetry at both 900-eV and 1200-eV re-emission photon energies.

Viewfactor calculations were in agreement with the experimentally measured hohlraum radiation flux and re-emit images when assuming 50% inner-beam and 95% outer-beam coupling

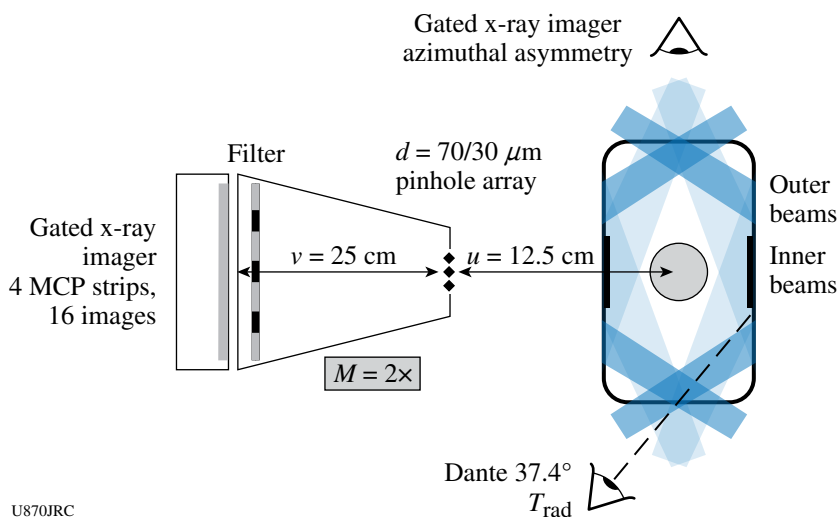


Figure 116.66
The re-emit experimental setup for the NIF and OMEGA.

U870JRC

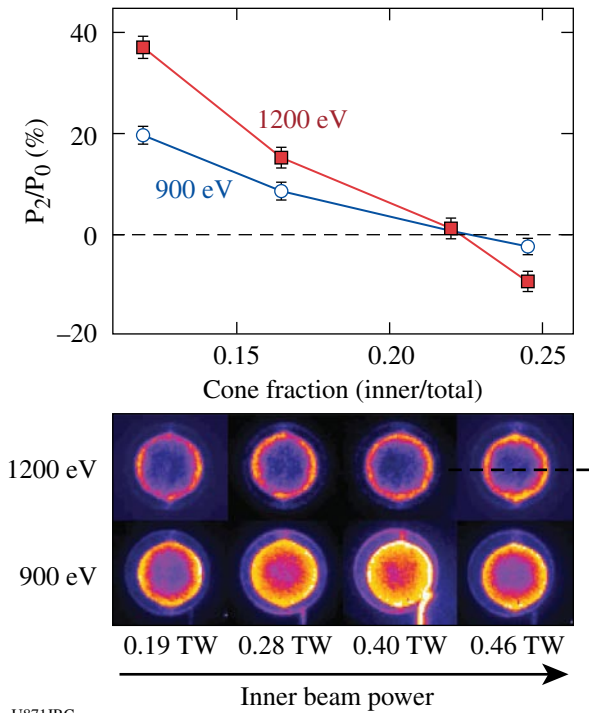


Figure 116.67
Re-emit images measured at 0.8 ns at 900-eV and 1200-eV energy bands for constant 0.28-TW outer-beam power and variable inner-beam power, and the corresponding measured re-emitted P_2/P_0 versus laser-cone power fraction.

into x rays at the hohlraum wall (Fig. 116.68). Radiation-hydrodynamic simulations used to design the NIC ignition target confirm the lower inner-beam coupling to within 10%, as do the thin-walled shell experiments described below.

Symmetry Diagnosis by Thin Shell: Should it prove necessary to further optimize the symmetry during the second and third shocks to obtain maximum yield, the shape of a thin-shell capsule in flight can be measured during this time period by x-ray backlit imaging. The thin shell will be made of the ignition ablator mate-

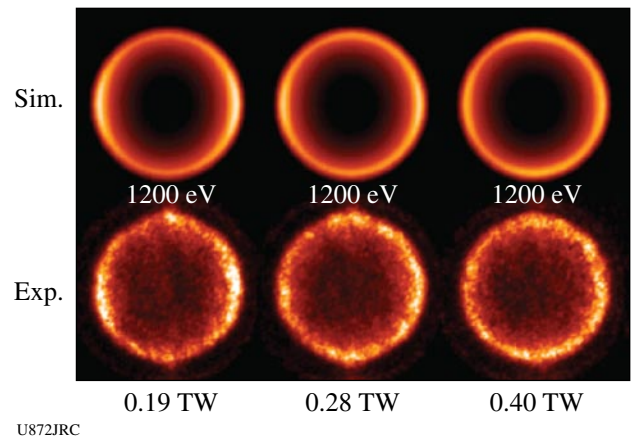
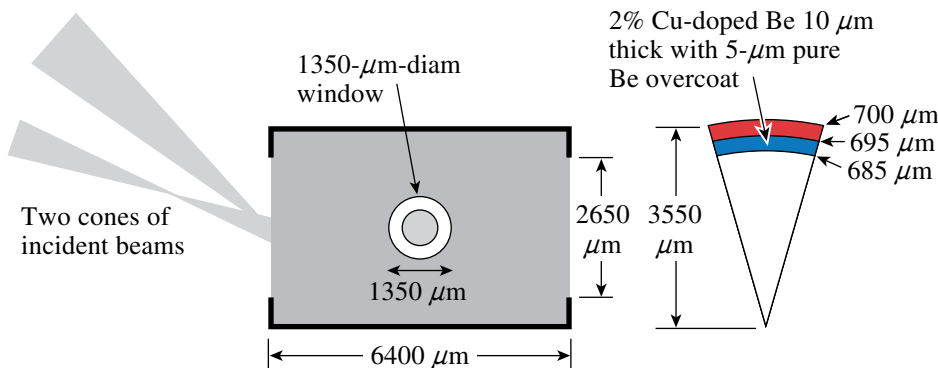


Figure 116.68
Simulated viewfactor versus measured re-emit images for different inner-beam powers (outer beams: 0.28 TW/beam).

rial with its thickness adjusted to optimize its sensitivity to drive at different times during the foot of the pulse. Recent experiments at the OMEGA Laser Facility demonstrated the viability of area backlit images of 0.6-scale Be capsules doped with 2% Cu under NIC foot conditions by using a 1-ns pulse shape for both drive and backlighter beams, as shown in Fig. 116.69.

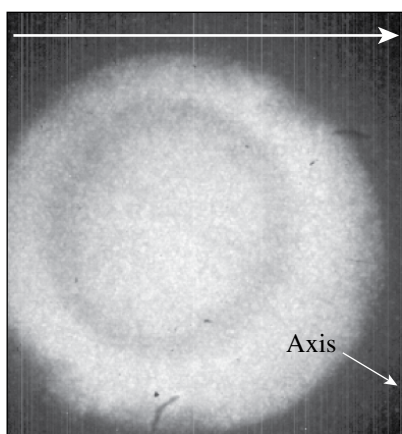
To determine the drive symmetry during the foot of the pulse, a scale-0.6 hohlraum was illuminated with a 1.0-ns pulse, giving a drive peaking at 125 eV early in time. Sixteen high-precision images of the converged shell were then recorded on each shot with a 4.7-keV (Ti) foil backlighter, at times between 6.6 and 7.4 ns; an example is shown in Fig. 116.70.

The sensitivity of the measured P_2 distortions to changes in the fraction of the power in the inner and outer cones of beams confirmed the predictions of simulations, as shown in Fig. 116.71, albeit with an offset consistent with 10% less inner-cone absorption than predicted by this simulation. The



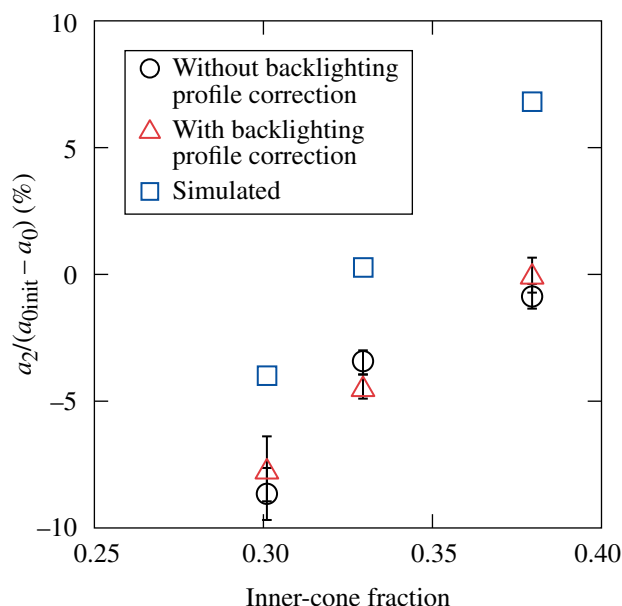
U873JRC

Figure 116.69
Schematic of the scale-0.6 NIC hohlraum and thin-shell capsule used on OMEGA to validate the plans to control the drive symmetry during the foot of the ignition pulse where $T_r \geq 100$ eV. The obtained backlit images demonstrated that the measured ball distortion has the expected sensitivity to the $\ell = 2$ component of the drive and can measure the Legendre moments to the needed precision.



U874JR

Figure 116.70
Image of a thin shell converged to half its initial radius by a 125-eV x-ray drive in the NIC-like hohlraum.



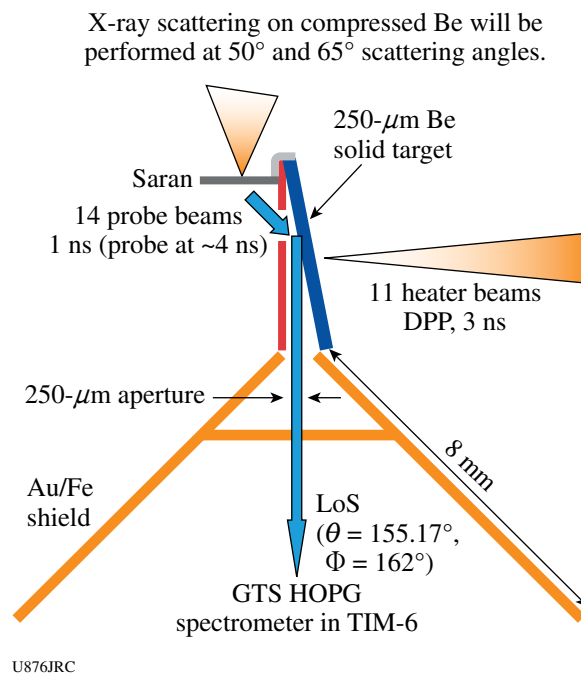
U875JRC

Figure 116.71
Measured versus simulated thin-shell P_2 relative to distance traveled versus cone fraction.

results verified that the overall measurement accuracy ($\pm 1\%$ in P_2 , extrapolating to $\pm 0.3\%$ at full NIC scale and larger distance traveled) is sufficient to meet the $\pm 0.5\%$ P_2 requirement for foot symmetry control in the NIC.¹⁷

X-Ray Thomson Scattering (XRTS) Conductivity: The ultimate goal of this campaign was to measure the plasmon broadening in collective x-ray Thomson scattering (XRTS) to extract the plasma collisionality and, therefore, conductivity,

which is important to accurately model capsule performance on the NIF. For this purpose, 250- μm Be foils were driven at $3.5 \times 10^{14} \text{ W/cm}^2$ over a total duration of 3 ns (see Fig. 116.72). From 1-D hydrodynamic simulations (*HELIOS*) we expected shock-compressed electron densities between 6 and $8 \times 10^{23}/\text{cc}$ and electron temperatures in the range of 10 to 15 eV at times ≥ 4.25 ns after the start of the heater pulse at the Be rear surface. The Cl Ly- α line at 2.96 keV was employed to probe the plasma parameters. The scattered signal was dispersed by the GTS HOPG spectrometer in TIM-6 and recorded by XFRC4 coupled to the LLNL charge-coupled device (CCD).

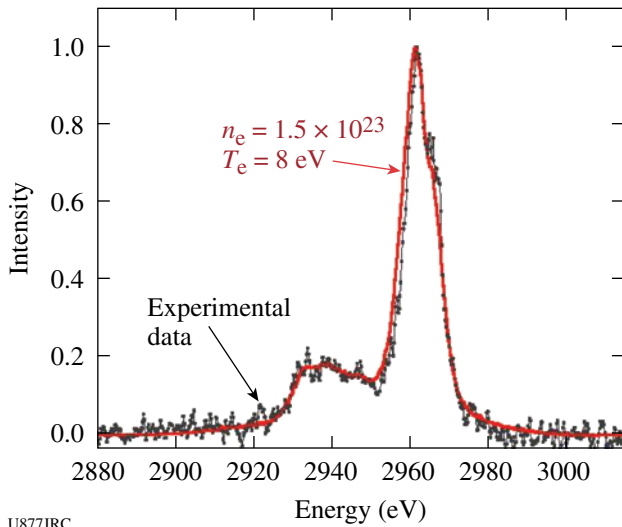


U876JRC

Figure 116.72
Schematic of the experimental configuration.

Figure 116.73 shows both the recorded spectrum from a 50° scattering shot fitted by a synthetically generated spectrum corresponding to a plasma density of $n_e = 1.5 \times 10^{23}/\text{cc}$ and an electron temperature of 8 eV. We note that the shape of the red-shifted plasmon was sensitive to both n_e and T_e , and that T_e , on its own, was sensitive through detailed balance to the ratio of the blue- to red-shifted plasmon.

The density was $4\times$ to $5\times$ below the values predicted by the hydrodynamic simulations. This suggests that either the shock speed was slower than predicted, leaving an uncompressed, possibly preheated, region probed, or that a low-density blow-off plasma was generated at the back surface, delaying shock breakout. In either case, the 2.96-keV Cl Ly- α radiation was

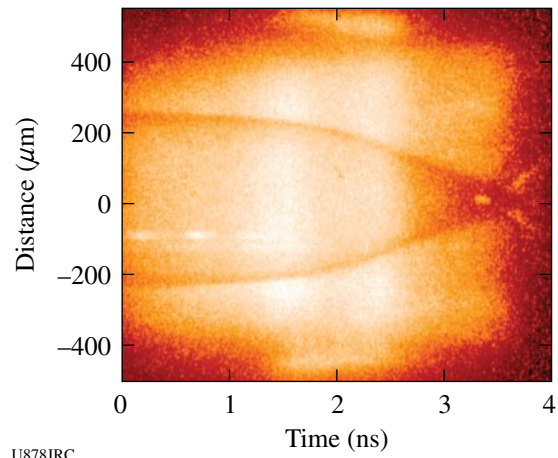


U877JRC

Figure 116.73
Experimental spectrum fitted to synthetic spectrum corresponding to $n_e = 1.5 \times 10^{23}/\text{cc}$ and $T_e = 8 \text{ eV}$.

unable to penetrate to the shocked region and out of the target again. Future shots will optimize target and probe design.

Convergent Ablation: Determining ablator performance during an implosion was a critical part of the NIF tuning campaign. In particular, it was vital to have accurate, in-flight measurements of the velocity, areal density, and mass of the ablator. In tests on OMEGA, a new technique was developed that achieved time-resolved measurements of all these parameters in a single, area-backlit, streaked radiograph of an indirectly driven capsule (Fig. 116.74). Abel inverting the absorption profile to determine the density profile at each time step accomplished this. Results

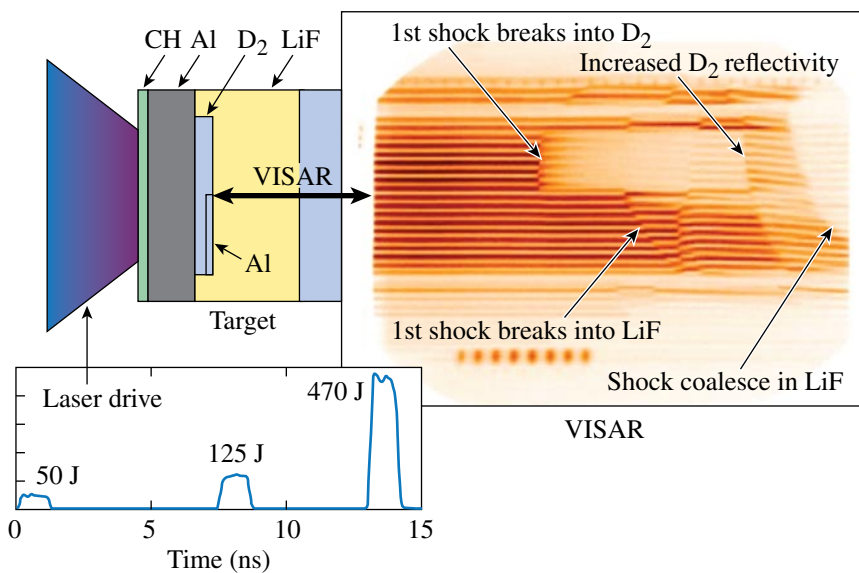


U878JRC

Figure 116.74
Streaked radiograph showing a converging capsule leading up to bang time at 3.3 ns.

showed a clear difference in ablated mass for Cu-doped Be-capsule implosions with different initial shell thicknesses, illustrating that this technique was suitably precise to be used as a remaining mass diagnostic for the NIF tuning campaign.

Deuterium Thermal Conductivity: Multiple shocks reverberating in a thin layer of liquid deuterium made it possible to attain quasi-isentropic compression of deuterium. Simultaneous measurements of velocity, reflectivity, and emissivity were used to investigate the transport properties of compressed deuterium. As seen in Fig. 116.75, the onset of a more highly reflective state at a temperature of 4000 K and pressure of 1.5 Mbar demonstrated a phase transition to a highly conductive, metal-like phase.



U879JRC

Figure 116.75
Experimental setup and VISAR record of shocked liquid D_2 .

Capsule Instability Seeding by Shock Nonuniformity: The CAPSEED campaigns performed measurements of fluid-velocity nonuniformities created by microscopic perturbations in NIC ablator materials. Begun in FY07 and continued through FY08, these campaigns employed a newly commissioned instrument—the OMEGA high-resolution velocimeter (OHRV)—as the primary diagnostic. During FY08 we carried out a survey of the three candidate NIC ablators: Cu-doped Be, polycrystalline diamond, and Ge-doped CH. In addition, much progress was made on analyzing of the data sets and extracting quantitative results. The experiments in October 2007 focused on microcrystalline diamond samples, Be(Cu) targets with preimposed ripples, and sections of capsule shells made from both types of target. Analysis of the rippled Be(Cu) targets showed good agreement between the measured shock-ripple amplitude and simulations of the time evolution of the ripple perturbation (Fig. 116.76).

A surprising result was finding that the shock-front nonuniformities produced by diamond samples shocked below the melt transition were significantly higher than the nonuniformities produced by the same material shocked into the solid–liquid coexistence region (Fig. 116.77). Further experiments in February studied Be targets shocked into the solid–liquid coexistence region, on polycrystalline diamond samples with nanometer-sized grains and on CH(Ge) targets. A third campaign in

April continued to examine the three ablator candidates, with a particular focus on Be(Cu) flats constructed with the layered Cu-doping scheme that is specified in the NIC point design for Be capsules. Results from these campaigns are being used to assess the different ablator candidates.

2. High-Energy Stewardship Experiments

Material Properties: In FY08, the Materials Strength Experimental Team performed two types of experiments on OMEGA: vanadium Rayleigh–Taylor (VRT) strength measurements and ramped-drive-development experiments that use indirect x-ray illumination from a hohlraum.

The VRT experiment tested models of material strength by measuring the Rayleigh–Taylor (RT) growth factors on accelerated sinusoidally rippled samples of polycrystalline vanadium.¹⁸ When driven, the amplitude of the rippled interface will grow via the RT hydrodynamic instability, with the amount of growth depending on the drive conditions and vanadium material strength at high pressures and strain rates. The amount of growth will be derived from face-on radiographs taken with the laser-driven x-ray backlighter. Our experiments were conducted to confirm the drive and growth-factor measurements of the previous experiments and to understand the results in terms of various material-strength models. The ripple sample had a period of 60 μm with an initial amplitude of

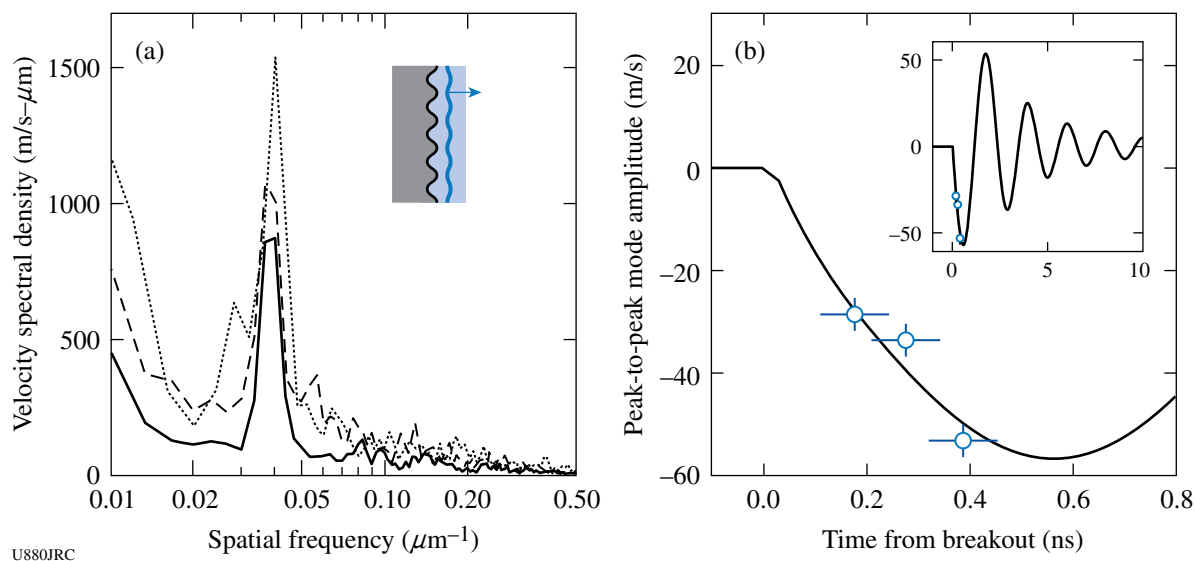


Figure 116.76

(a) Velocity spectra recorded at 180 ps (solid), 280 ps (dashed), and 390 ps (dotted) after shock breakout recorded from targets with a preimposed sinusoidal ripple of 25- μm wavelength and 125-nm initial amplitude at the interface between the Be(Cu) ablator and the PMMA indicator material. The 25- μm ripple mode occupies the spectral peak near a 0.04- μm^{-1} spatial frequency. (b) Velocity amplitude of the isolated ripple modes (symbols) compared to the prediction from a hydrodynamic simulation (curve). Inset: the same data on an expanded time scale.

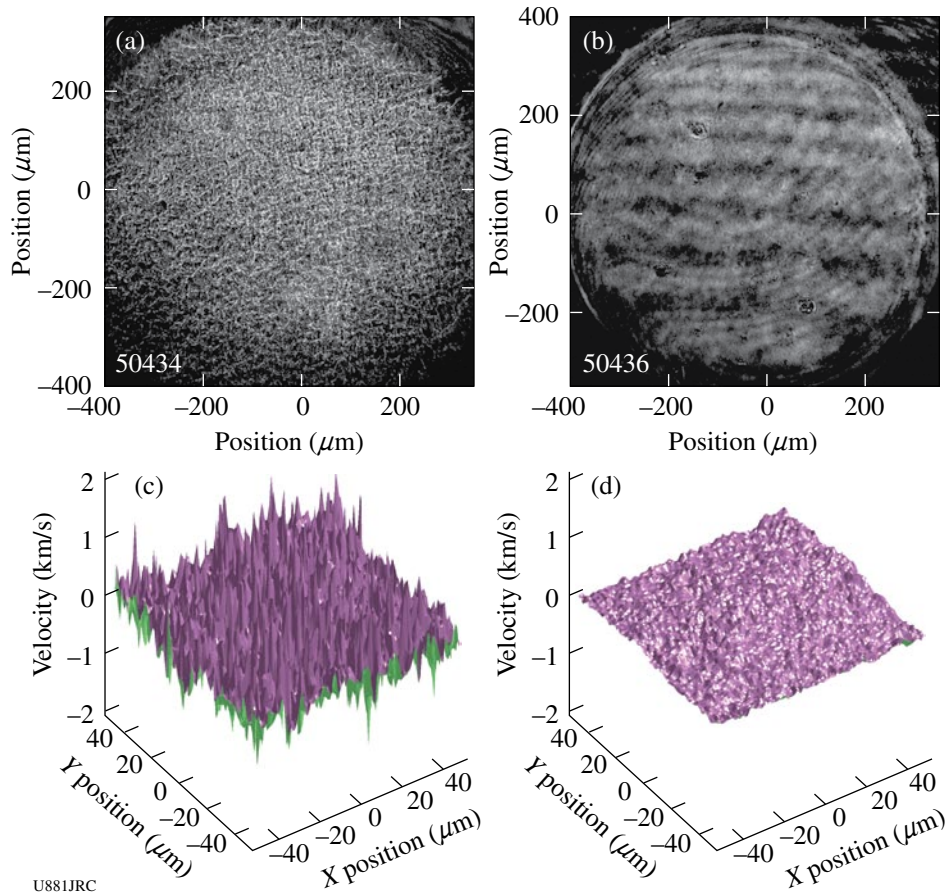


Figure 116.77

Intensity patterns of the probe beam reflected from shock fronts transmitted through polycrystalline diamond samples: (a) at ~ 300 GPa, which is below the melt, and (b) at ~ 800 GPa, which is in the solid–liquid coexistence region. Two-dimensional spatial-velocity fluctuations extracted from a $50 \times 50 \mu\text{m}^2$ region of these datasets are shown in (c) and (d), respectively.

$0.6 \mu\text{m}$. Figure 116.78 shows a radiograph of the ripples at 70 ns after the start of the drive using a vanadium He- α backlighter (~ 5.2 keV). From these data, we derived a measured growth factor of 12. Our data were compared with hydro simulations using three different strength models. The models we studied were Steinberg–Guinan (SG), Preston–Tonks–Wallace (PTW), and the new multiscale model that was developed at LLNL by Arsenlis and Becker. Figure 116.79 shows the results. We found that, in all cases, our measurements required modification to the model input parameters. With these modified input parameters, however, all three models were brought into agreement with the measurement. An experimental campaign over several different pressures and strain rates would now be required to distinguish between the models.

We performed three additional experiments that developed isentropic drives using hohlraums to drive a reservoir-gap-sample target package.¹⁹ We employed an extended scale-2.5

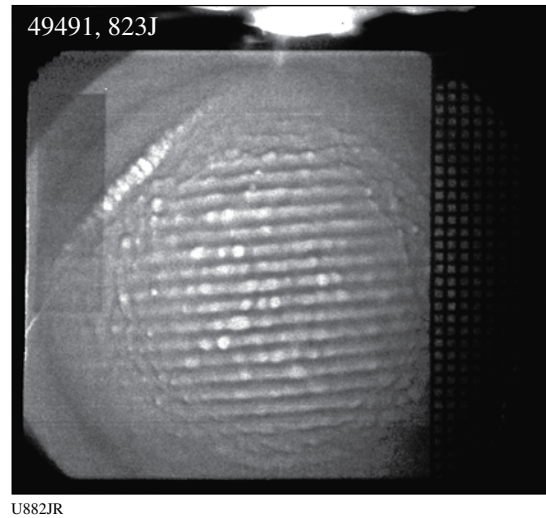
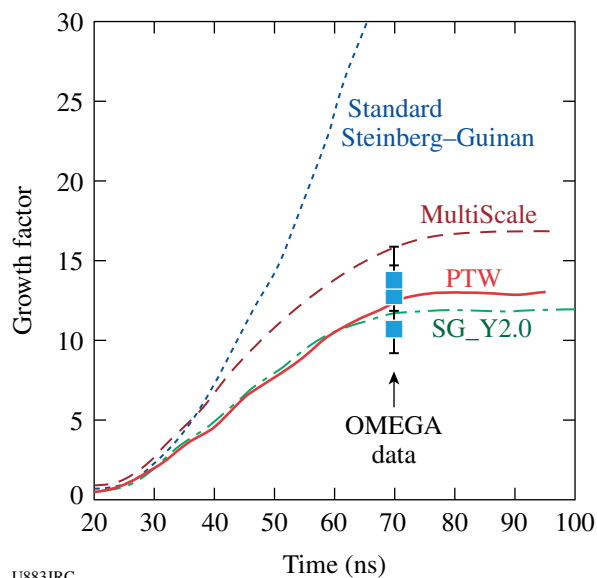


Figure 116.78
Vanadium Rayleigh–Taylor ripple-growth image taken 70 ns after the drive.

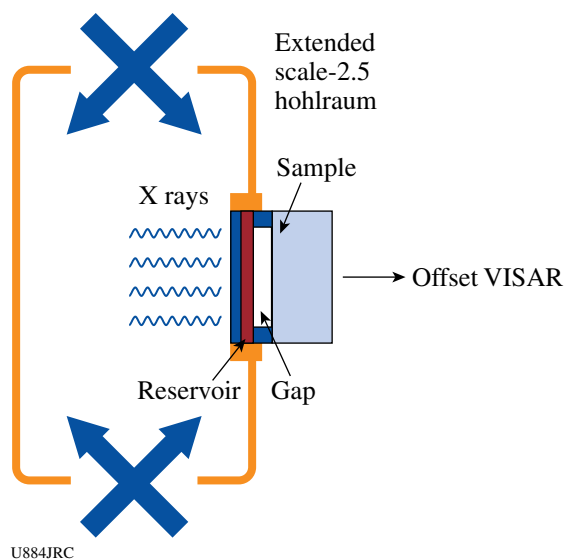


U883JRC

Figure 116.79

Experimental results (solid squares) of the vanadium ripple-growth factor versus the predictions from three different strength models. All models required changes to parameters to fit the data. Experiments at different pressure or strain rates will make it possible to distinguish the differences between the models.

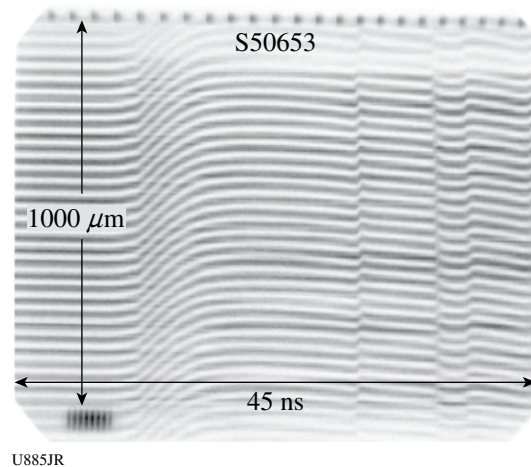
hohlraum (7.0-mm length, 4.0-mm diam; and 2.4-mm-diam LEH) for the first time to create large enough planar regions to drive our samples in a ramp-loading configuration. We used the active shock breakout (ASBO) offset telescope that was specifically designed and commissioned to measure the pressure profile of samples mounted on the equator of the hohlraums. A schematic of our hohlraum package is shown in Fig. 116.80. The reservoir was a 75- μm -thick CH ablator glued to a 200- μm -thick 12% BrCH. An example of the resulting velocity interferometer for any reflector (VISAR) image from this hohlraum is shown in Fig. 116.81. Our measurements showed that the planarity in the measured data yielded resolution better than 150 ps across the entire 1-mm field of view. The peak radiation temperature (T_r) of 130 eV, measured by Dante, agreed well with the simulations. We also observed, however, unexpected second and third pressure rises and a late-time stagnation shock, as shown by the dashed-dotted curves in Fig. 116.82. Since our RT strength experiment requires taking radiographs at late times (>50 ns), these additional pressure waves and shock will cause undesirable increases in the growth factors. Our current understanding of these additional pressure rises is that they are caused by late-time hohlraum radiation, after the laser turns off. The experiments suggest that this late-time radiation (T_r) in the “tail” of the drive is ~ 15 eV higher than predicted by *LASNEX*.²⁰ This causes additional late-time ablation pressure, which recompresses the package



U884JRC

Figure 116.80

A schematic of a quasi-isotropic drive target package mounted on a scale-2.5 hohlraum.

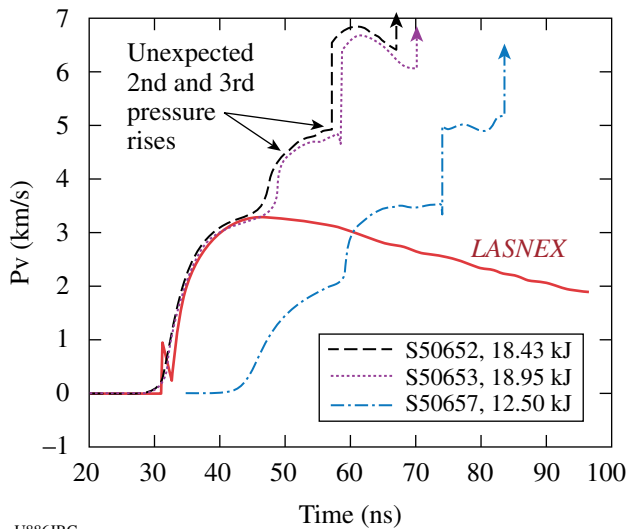


U885JR

Figure 116.81

A VISAR image of the hohlraum-driven quasi-isotropic drive. The planarity yields resolution better than 150 ps across the 1-mm field of view.

and launches additional pressure waves. The strong, late-time shock indicated by the “up” arrows is thought to occur because the ablated plasma from the ablator is flowing into a confined volume (the hohlraum), which fills up with plasma and exerts a back pressure, as opposed to flowing into an infinite vacuum, as modeled by *LASNEX* (solid curve in Fig. 116.82). This is called the stagnation shock. We artificially modified the simulated T_r profile so that it preserved the peak T_r , but increased the late-time T_r profile; the drive profile was roughly reproduced from this experiment.



U886JRC

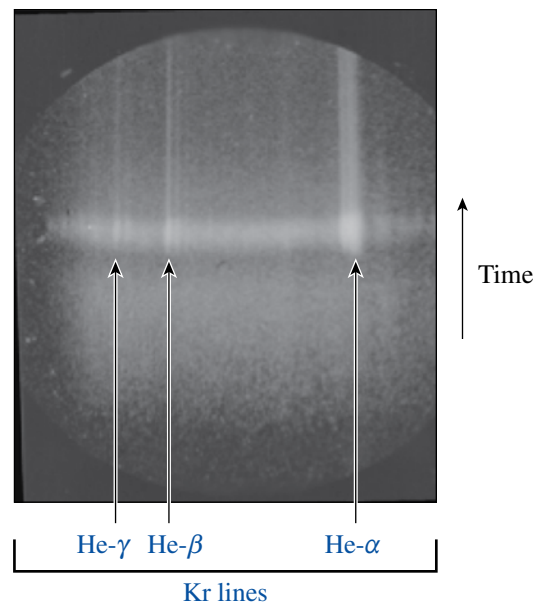
Figure 116.82 Drive profile from the hohlraum-driven ramped drive. The second and third rises are likely caused by late-time T_r that causes additional ablation pressure. We are now investigating the thin-walled hohlraums ($<1\text{-}\mu\text{m}$ Au layer) to delay these late-time pushes.

We also tested a reservoir comprised of layers of high-density (1.98 g/cm^3 12% BrCH) to low-density (1.41 g/cm^3 4.3% BrCH) brominated plastic to test if hydrodynamic instabilities at the interfaces in the reservoir caused an unacceptable spatially nonuniform drive. The VISAR results showed that there is no spatial nonuniformity from these layers. We also tested quartz as a possible reservoir material. To reach very high pressure ($>10\text{ Mb}$), a high-density, high-sound-speed material will be needed as a part of the reservoir. These experiments will need to be performed on the NIF, where a high enough temperature can be achieved to generate the required plasma drive on release.

We studied a 500-mg/cm^3 foam layer that will be a part of the reservoir for the 5-Mb Ta strength experiment on the NIF. The low-density foam layers will make it possible for smoother loading of the initial ramp profile, thus mitigating the initial shock that may cause the sample to melt. It was demonstrated that the 500-mg/cm^3 CRF foam properly released into vacuum and did not display any spatial nonuniformity. The shock-breakout times from the foam, the release temperature, and arrival time across the gap matched the LASNEX predictions well.

In FY09, drive development will be continued using thin-walled hohlraums designed to lower the late-time T_r (Ref. 21). There are plans to perform Ta RT experiments using OMEGA EP's $>20\text{-keV}$ backlighter capability.

Non-LTE Implosions: The goal of the nonlocal thermodynamic equilibrium (NLTE) campaign is to build a platform to study energy balance in implosions by measuring ion, electron, and radiation temperatures as a function of high-Z dopant concentration. In FY08 experiments, 60 beams of OMEGA were used for direct-drive implosions of thin ($4\text{-}\mu\text{m}$) glass capsules filled with 10 atm D^3He gas and 0.005 atm Kr gas as a spectroscopic tracer. The relative concentration of DD and ^3He was varied during the shots, and some capsules also contained as much as ~ 0.1 atm Xe. As a time-resolved electron-temperature (T_e) diagnostic, we fielded a mica conical crystal spectrometer coupled to a streak camera and viewed K-shell emission lines from the Kr dopant (see Fig. 116.83). Time-integrated spectra were also recorded with the HENEX spectrometer developed by NIST/NRL. We also fielded the direct-drive multispectral imager (DDMMI) to obtain 2-D images in the light of Li-like Kr lines. An increase in the DD/DDT yield ratio with increasing DD concentration was observed, as well as an increase in the ion temperature, inferred from proton and neutron emission-time histories and spectra. The continuum emission spectra recorded from HENEX have been used to infer the time-integrated electron temperatures, which show a temperature decrease with an increase of dopant concentration. We used the time-resolved spectra from the conical crystal spectrometer to study the temporal evolution of the Kr He- β lines. The He- β_2 /He- β_1 line ratio shows a peak in the central 50 ps of the Kr emission. Data analysis and comparison to simulations



U887JRC

Figure 116.83 Typical time-resolved spectrum from the mica conical crystal spectrometer, for a capsule without Xe dopant.

is ongoing. For the next campaigns, we are building a Johann spectrometer, which will use the Doppler broadening of x-ray lines for measuring ion temperature (T_i), and a new multimono-chromatic imager (MMI) designed for narrowband imaging in the 8- to 15-keV spectral region.

Long-Duration Backlighters: The long-duration backlighter campaign successfully demonstrated a pinhole-apertured point-projection backlighter lasting for 8 ns at both the Ni He- α -line energy (7.9 keV) and the Zn He- α -line energy (8.9 keV) (Ref. 22). Experiments on OMEGA used 20 beams with 1-ns square pulse shapes from P₇, with individual beams delayed such that the laser intensity on target was 2.6 to 2.9×10^{15} W/cm² for 7 ns, and 1.6×10^{15} W/cm² for an additional 1 ns. Beams irradiated either a zinc or nickel microdot, mounted on a 400- μ m-thick high-density carbon substrate, centered over a 20- μ m-diam pinhole or a 20- μ m \times 200- μ m slot aperture in a 75- μ m-thick tantalum substrate, with the target normal along the P₆-P₇ axis. The resulting x rays imaged a gold grid or wire array at 20 \times magnification on either a framing camera or streak camera in TIM-4. Diagnostics also monitored the emission spot, x-ray conversion efficiency, backscatter, and hard x-ray production.

Resolution studies on both gated and streaked diagnostics confirmed little-to-no pinhole closure over 8 ns for the nominal target and beam setup, which fired outer-cone beams first. Rearranging beams such that inner-cone beams fired first gave better conversion to x rays, which may have caused the pinhole to close

faster, but gave a dimmer overall signal late in time, resulting in dim images that could not be analyzed for source resolution. Early-time results on those shots showed very little pinhole closure. Figure 116.84 shows a streaked image of a wire array, illuminated with a nickel microdot emitter with a slot-apertured backlighter over 8 ns, and a lineout in time of the signal. Notice the signal varies some as beams turn on and off over the 8 ns. The laser intensity on target is relatively constant over the image, but beams closer to normal to the target's surface convert better to x rays. This can be seen by comparing the signal level early in time in the image, when 58 $^\circ$ beams were on, to late times in the image, when the 21 $^\circ$ beams fired.

Additionally, gated tests were done to purposefully cause quick pinhole closure, to match *LASNEX* models of closure time. The standoff distance between the microdot emitter and the pinhole was reduced to 250 μ m, which was irradiated with a 3×10^{15} -W/cm² laser source for 5 ns by 21 $^\circ$ and 42 $^\circ$ beams. Resolution of grid wires and change in signal level through the pinhole show that the pinhole was closed to a 7 ± 2 - μ m-diam source in 2.25 ns.

X-Ray-Source Applications: Bright, tunable x-ray sources are necessary for radiography applications, radiation-effects experiments, and as backlighters for high-energy-density experiments. LLNL's x-ray-source development campaign had one full day of shots during which three varieties of a multi-keV x-ray source were shot.²³ The x rays from the laser targets were characterized as a function of different

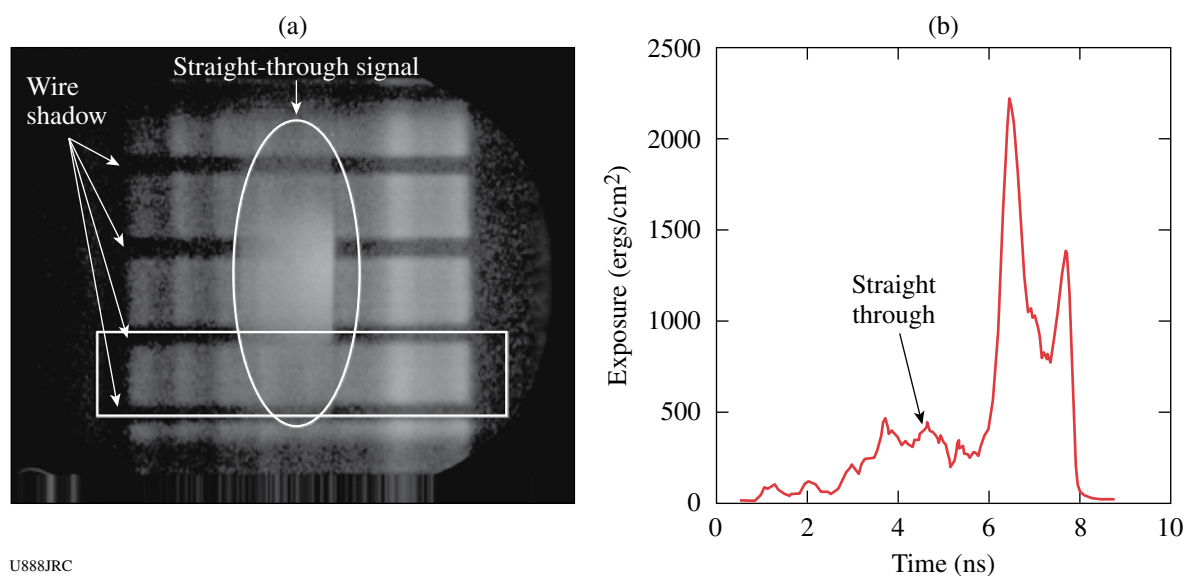


Figure 116.84
A streaked image of a wire array, illuminated with a slot-apertured backlighter over 8 ns with a nickel microdot emitter, and a lineout in time of the signal.

target geometries and volumes. Previous campaigns studied target yield as a function of laser intensity and target-plasma density. The x-ray sources were created by driving (using 20 kJ of laser energy) either ultralow-density (3- to 4-mg/cm³) Ge-doped (20% atm) SiO₂ aerogels or Ge-foil-lined epoxy (CHNO) cavities. The laser-to-x-ray conversion efficiency in the 10- to 13-keV x-ray band was measured to be between 0.6% and 1.0% and in the 1.0- to 3.5-keV band between 35% and 40%. These shots compared output from aerogel targets that differed by 40% in volume and saw no difference in the measured x-ray yields. X-ray spectra and time-resolved images of the three types of targets are shown in Fig. 116.85. Analysis indicated that the laser-heated volume was the same in both targets, which resulted in the same number of emitting ions in the plasma. Similarly, and surprisingly, the foil-lined cavities produced measured yields, in all spectral bands, that did not differ from those of the aerogel targets. The measured yield for the foil-lined cavity target was consistent with trends observed with previous cavity targets, shot in 2007 by Commissariat à l'Énergie Atomique (CEA) researchers, that produced higher yields and had a better-optimized laser configuration. These experiments were conducted jointly with U.K.'s Atomic Weapons Establishment (AWE) Laboratory, Sandia National Laboratories, France's CEA, and the Department of Defense's (DoD) Missile Defense Agency and Defense Threat Reduction Agency. The x rays from these targets were applied to various test objects and the response was measured.

Dynamic Hohlräume: Earlier experiments showed that laser-driven dynamic hohlraums (LDDH's) emit very bright, spectrally smooth bursts of x rays up to 3.5 keV, suitable as broadband backlighters for absorption spectroscopy experiments (Fig. 116.86). These experiments also demonstrated that LDDH's are robust

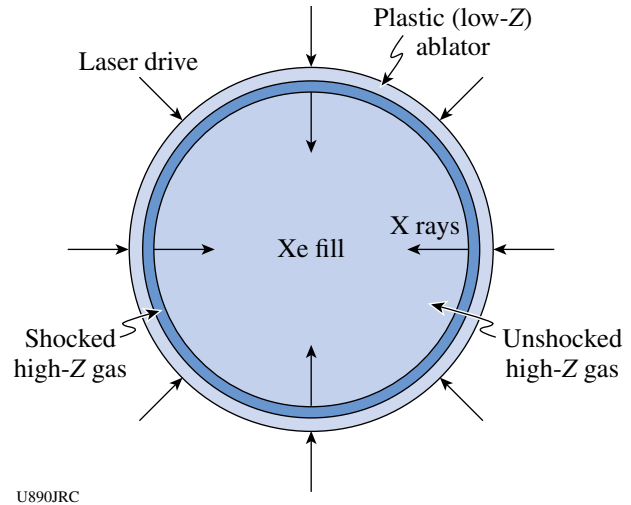
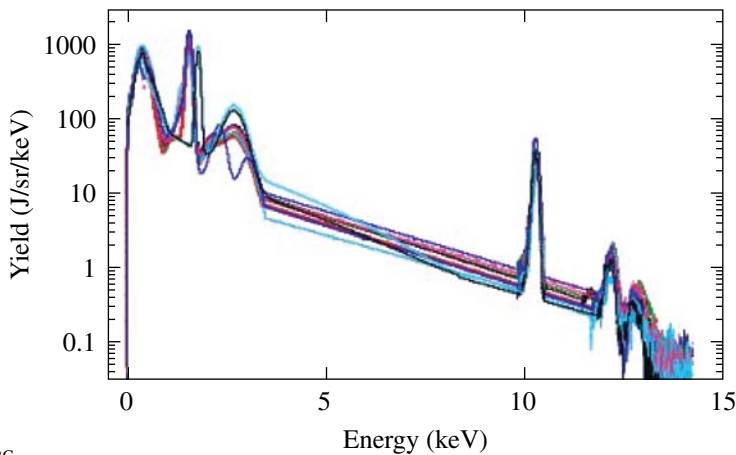


Figure 116.86 Concept of “dynamic hohlraum”: shock-heated Xe gas forms a spherically converging shell that traps radiation inside. When the shell stagnates, radiation is released in a bright x-ray flash suitable as a backlighting source for opacity experiments. Data obtained of the converging dynamic hohlraum included x-ray streaked images of the self-emitted x rays, multiple x-ray images, and spectral data.



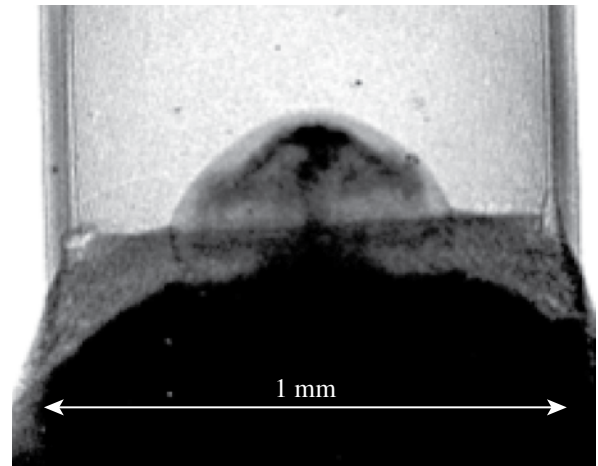
Figure 116.85 (a) Time-integrated x-ray pinhole-camera images, filtered for x rays above 3 keV, of the large and small aerogel targets shot on the x-ray source development day (8 May). (b) X-ray spectra reconstructed from data measured with the HENWAY spectrometer and the Dante diode array. Across the whole range shown, 35% to 45% of laser energy is converted into x rays.



U889JRC

to the polar (nonspherically symmetric) laser configuration that will be used on the NIF as a continuum source backlighter. During FY08, these two aspects of LDDH's were combined in an experiment where a Xe-filled LDDH without an inner shell was driven by laser beams in a polar configuration and was used as a backlighter for absorption spectroscopy of heated Fe samples.²⁴ It was found that the LDDH emits a strong, 200-ps-long x-ray flash that is spectrally smooth from 4.5 keV to ~9 keV, enabling a significant expansion of the spectral range for future OMEGA and NIF opacity experiments. This year's LDDH experiments also completed a series of shots where capsules were filled with neopentane rather than xenon. These shots were experimentally difficult as the gaseous neopentane was near its boiling point just prior to the experiment and condensation had to be avoided. The successful completion of the experiment made it possible to measure the difference in yield and fuel density caused by the hohlraum effect (which is present in "standard" xenon-filled LDDH's but not in neopentane).

High-Speed Jets: The evolution of high-speed jets is an important benchmark for hydrodynamic simulations, e.g., the shape of the front of a jet penetrating into a surrounding medium can be either flat-topped or arrow-shaped, and this must be correctly predicted by simulations. An OMEGA experiment yielded a dramatic increase in the current data set of high-speed-jet images; the evolution of the jet was followed temporally ~2 to 2.5× longer than in previous experiments on OMEGA and in the NIF Early Light campaigns (see Fig. 116.87). A preliminary result from the experiment is the need to model foam material as two fluids in numerical simulations. A new

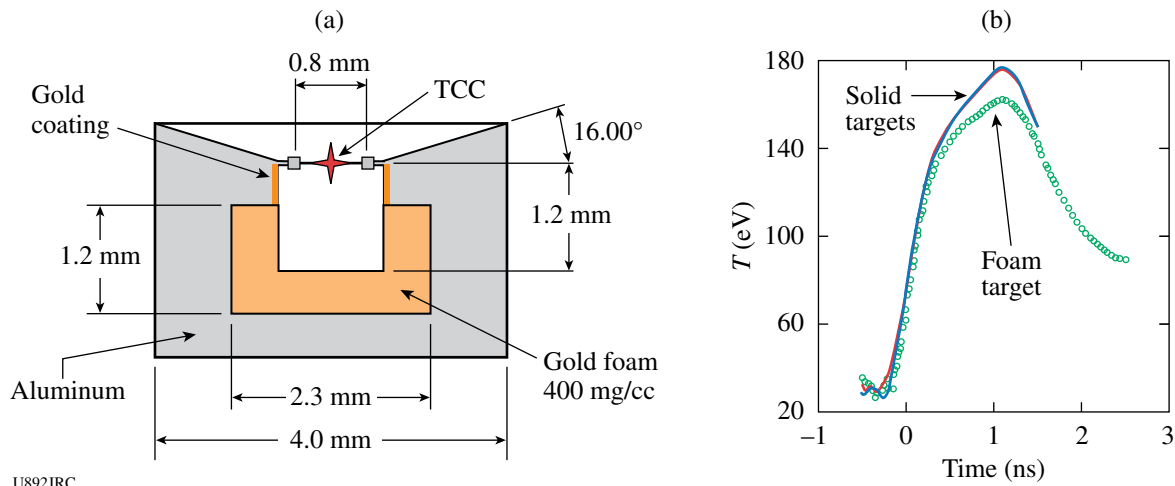


U891JR

Figure 116.87 X-ray radiograph of an aluminum jet driven into a 0.1-g/cm³ carbon foam. The image is taken 35 ns after the start of the experiment, and the jet has evolved ~2× longer than in previous experiments of this type. The jet structure is clearly visible, as is the location and shape of the bow shock.

two-fluid model for foams is currently under development at LLNL. In the new model, foam is treated both with LEOS (used for undisturbed foam) tables and with an ideal gas (used for foam that has been "reflected" by the shock, i.e., cast out ahead of the shock by shock-foam interaction forces).

Enhanced Efficiency Hohlräume: The hohlraum development campaign investigated the behavior of gold-foam-walled halfraums ($\rho = 400 \text{ mg/cm}^3$), comparing the flux levels and temperature to solid-gold halfraums.²⁵ The layout of the foam-walled halfraum is shown in Fig. 116.88. By optimizing the wall



U892JRC

Figure 116.88 (a) Gold-foam-walled halfraum-target schematic. Beams hit a gold-coated plate near the LEH, while the rest of the cavity is lined with 400-mg/cm³ foam. (b) Temperature as a function of time for two solid-gold targets and one foam target. Although lower-density gold was predicted to optimize target flux and temperature, the foam target had a lower temperature than the solid targets.

density for these hohlraums at temperatures near 200 eV, we expected to see an increase in flux by $\sim 15\%$. These shots positioned the targets on the Dante axis and used 15 beams from the H16 direction, with the RR1001 reverse-ramp pulse shape and IDI-300 phase plates. Beams hit a 1200- μm -diam gold-coated solid surface near the 800- μm LEH on the foam targets, which hid the laser spots from the Dante view. The inner foam or solid surface was 1200 μm in diameter and 1200 μm in length. Dante measured flux while a soft x-ray camera in TIM-6 monitored the LEH. Over three shots, two solid targets were compared to one foam target. These shots showed a lower flux in the foam target than in the solid targets, contrary to our predictions [see Fig. 116.88(b)]. We are investigating whether the reverse-ramp pulse shape was the appropriate choice. Remaining targets will be used for future tests.

Opacity: In FY08, LLNL completed the development of a high-temperature laser-opacity platform. Thin-foil samples of co-mixed sodium chloride and titanium, tamped by plastic on all sides, were placed inside hohlraums, and heated to temperatures well above 100 eV in local thermodynamic equilibrium, or LTE, conditions. The samples were then backlit by two different broadband radiation sources. Separate shots used samples of co-mixed tantalum and titanium. The data in Fig. 116.89 show an edge-on view of the sample, backlit by a ten-beam Kr-filled dynamic hohlraum capsule backlighter, which was apertured down to 30 μm in one direction to improve the spatial resolution. The data are spectrally resolved in the horizontal direction using an MSPEC elliptical crystal spectrometer and a gated microchannel-plate detector. This was the first-ever laboratory measurement of a hot sample in the photon energy range above 4 keV. The expansion of the sample was consistent with pre-shot *LASNEX* simulations and established the sample density. The spectrum was well fit by the *VISTA* opacity code, using the known optical path length and measured density, at a temperature of 110 ± 5 eV. Separate, nearly synchronous measurements were obtained in a 250- to 1600-eV spectral band using a variable-spaced grating spectrometer and a second backlighter. The latter data, including both absorption and self-emission spectra from the hot sample, provide detailed information on the sample's opacity in the spectral band contributing to the Rosseland mean opacity, which, in turn, controls the overall radiation flow through such a plasma. By simultaneously characterizing the sample's density, temperature, ionization balance, and Rosseland-band opacity, this new experimental platform makes possible detailed, photon-energy-specific investigations of the process of radiation transport in the hot plasmas found deep inside the sun and other stars.

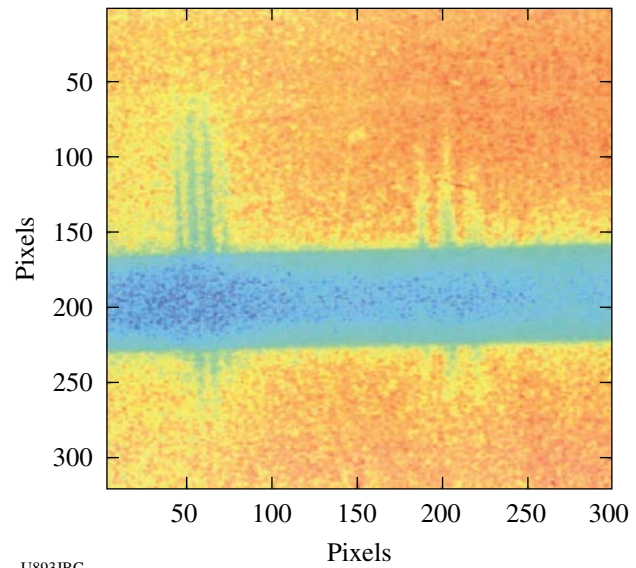


Figure 116.89

Gated space-resolved titanium absorption spectrum for photon energies around 5 keV. The horizontal bar is a gap between two strips on the detector. To the left are $n = 1$ to 2 absorption lines of F-like to C-like Ti. To the right are $n = 1$ to 3 lines of the same ions. The spatial expansion of the sample is determined by the vertical extent of the lines.

FY08 LANL OMEGA Experimental Programs

During FY08 Los Alamos National Laboratory (LANL) successfully fielded a range of experiments on OMEGA to study the physics relevant to inertial confinement fusion (ICF) and high-energy-density laboratory plasmas (HEDLP) in support of the national program. LANL conducted a total of 85 target shots on OMEGA. Collaborations with LLNL, LLE, MIT, and AWE remain an important component of LANL's program on OMEGA.

AGEX-EOS: The AGEX-EOS-09 campaign studies the role that radiative preheating plays in the Richtmyer–Meshkov mixing of a large-Atwood-number interface. The experiment uses a variant of the off-Hugoniot platform to produce a heated interface that is subsequently shocked. The resulting interface evolution is imaged radiographically.

The new platform, first tested in September 2008, employs an independently controlled shock and heating drive as well as a point-aperture pinhole backlighter configuration. The primary objectives for the September campaign were to exercise this new platform under every permutation of drive, identify sources of noise, and demonstrate the imaging viability of the experiment.

Figure 116.90 shows the target geometry and preliminary data obtained from shot 52215. The data clearly show the posi-

tion of the heated and shocked Teflon interface as well as the positions of the main and preheat-side shocks at 25 ns. Drawing from the success of September's experiment, a number of imaging improvements have been initiated, giving us high confidence for the physics experiments planned in February 2009.

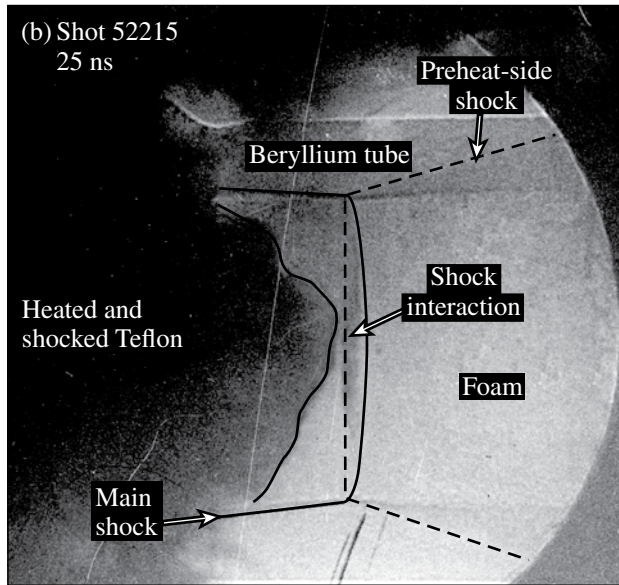
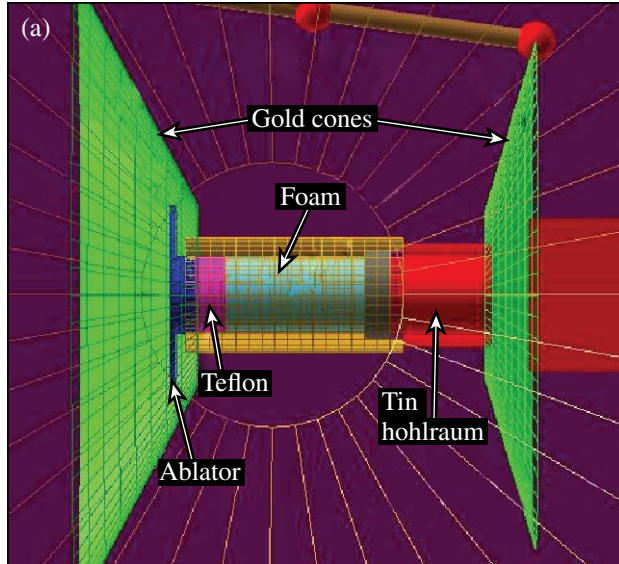


Figure 116.90 Overview of the (a) AGEX-EOS-09 target and the preliminary data from (b) shot 52215.

DTRat: In August 2008, LANL continued the *DT Ratio-³He Addition* campaign, imploding glass capsules filled with DT/³He using a 600-ps square laser pulse. Previous studies have looked at the effect of adding ³He to the D₂-filled capsules (as a

DT surrogate); this study is the first to look at the effect on DT. The use of DT also makes it possible to acquire high-quality reaction histories derived from the Gas Cherenkov Detector (GCD-1). From these reaction histories, it has been determined that the addition of ³He degrades the compression component of yield more than expected. This is consistent with the conclusions of the study conducted by MIT using D₂/³He-filled plastic capsules²⁶ and LANL's Hi-Z campaign utilizing glass capsules, also filled with D₂/³He (Ref. 27). Contrary to the MIT study, however, the shock component does not appear to be significantly affected.

Figure 116.91 shows the reaction histories for three concentrations of ³He addition. Overall, the measured neutron yield is ~37% of a clean calculation for *each* ³He concentration. However, when the histories are decomposed into Gaussian components representative of shock and compression yields, the measured compression component goes from being a factor of 3 lower than calculated at 0% ³He, to being a factor of 5 lower at 36% ³He. This agrees well with the MIT study as seen in Fig. 116.92 (the factor of 3 at 0% ³He is normalized out for the DTRat data set, whereas a factor of ~2.2 is normalized out for the "Rygg" data set). In contrast, the decomposed shock com-

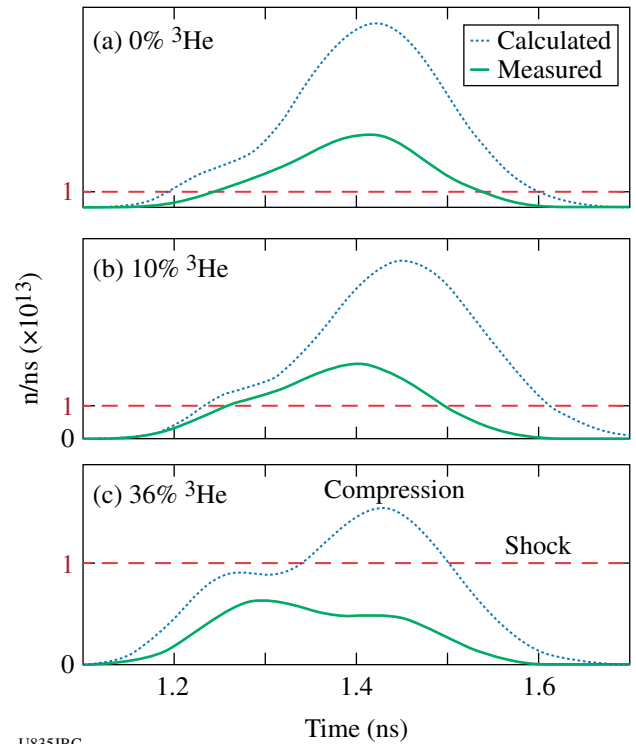
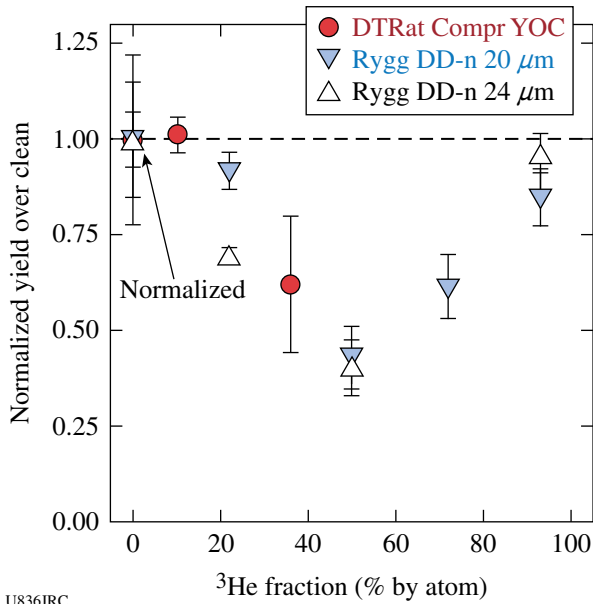


Figure 116.91 Calculated (convolved with residual instrument response) and measured (deconvolved GCD data) reaction histories for various ³He concentrations.

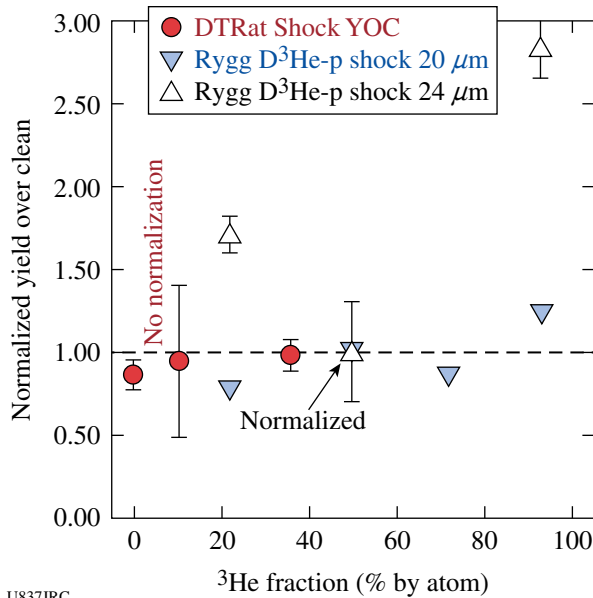


U836JRC

Figure 116.92
Scaled compression component of neutron yield normalized to 1 at 0% ^3He .

ponent from DTRat agrees quite well with the clean calculation for all three ^3He concentrations as shown in Fig. 116.93.

Shock-yield data for the 24- μm -wall-thickness capsules from MIT's "Rygg" study exhibit a parabolic dependence on ^3He fraction, with the minimum occurring near 50% ^3He ,



U837JRC

Figure 116.93
Scaled shock component of neutron yield normalized to 1 at 50% ^3He for "Rygg" data; no normalization for DTRat data.

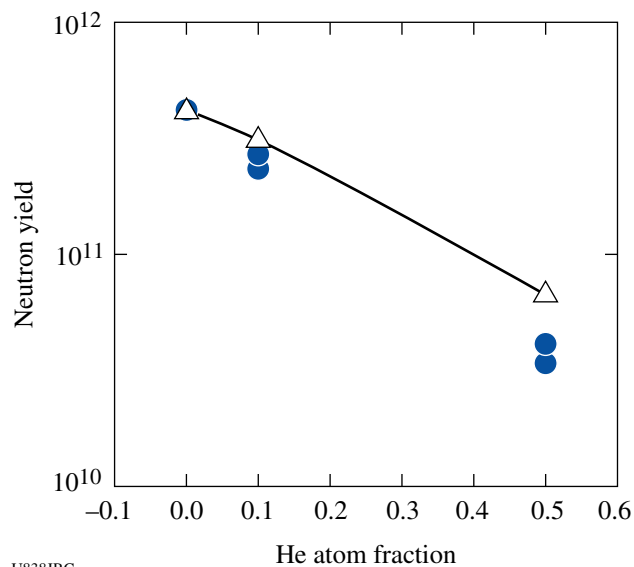
similar to what was observed for the compression component. The data set for 20- μm -thick walls, however, does not appear to support this trend. We suspect the degraded yield anomaly arises only after the shock has reflected from the center and has hit the incoming shell. After such time, the shock yield is diminishing while the compression yield is rising. X-ray imaging and ρR data from DTRat, Hi-Z, and the MIT study support the hypothesis that capsules with $\sim 50\%$ ^3He are not as compressed at the time of peak neutron production rate during the compression phase as those without ^3He (or those with nearly pure ^3He from the MIT study). It is not understood at this time what is degrading the compression.

High-Z: The High-Z project successfully completed its planned experiments for FY08 at the OMEGA Laser Facility. These experiments investigated what effect the addition of He to ICF implosions has on fusion yield. The experiment used the standard glass-shell targets we have used in the past and varied the concentration of ^3He in the target and measured the resulting yield. These were done for three different concentrations of ^3He : 0%, 10%, and 50% by atomic fraction. The gas fills were also designed to be hydrodynamically equivalent to try to ensure similar hydrodynamic behavior. In addition, we also planned to measure the change in yield for two different laser pulse lengths. We first used our standard pulse length of 1.0 ns and then conducted a second series of experiments using a shorter pulse length of 0.6 ns. The shorter pulse length should emphasize the differences in the compression component of the yield where we believe the ^3He is causing a significant impact.

On 23 April 2008, we successfully fired eight shots on OMEGA with 1-ns laser pulses and varied the concentration of He in the capsules. The neutron-yield results from these experiments are shown in Fig. 116.94, along with the expected degradation caused by less deuterium in the target. One can see in the figure that the observed yield does fall below the expected yield as the He is increased. We also see little difference in the ion temperature for these shots, which varies from 6.9 keV to 7.4 keV and increases only slightly as the He concentration is increased.

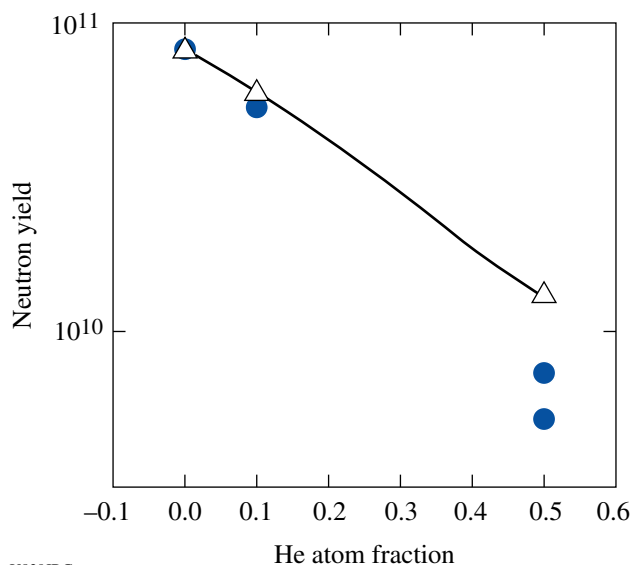
We also did two additional shots on 23 April with 4.0- μm -thick glass shells. These targets contained 50% atom fraction of He, but one was ^4He instead of the usual ^3He . The yields for these two shots were 4.8×10 and 4.3×10 , respectively—a difference of 10%, which is similar to our standard shot-to-shot variation. The ion temperature for these shots was higher, ~ 8.2 keV, consistent with thinner glass and a more rapid implosion.

Four additional shots were conducted on a separate half-day, 17 June; the results from those shots are shown in Fig. 116.95. The behavior is similar to what was observed for the 1-ns drive shots with one exception: the ion temperatures for these experiments varied greatly, from 5.3 keV for no He to 7.8 keV



U838JRC

Figure 116.94
Neutron yield as a function of He atom fraction in the gas. The dots are data for a 1-ns pulse drive with 4.3- μm -thick walls and the curve represents the expected yield based on the deuterium concentration only.



U839JRC

Figure 116.95
Neutron yield as a function of helium atom fraction in the gas. These experiments used 0.6-ns laser drive and the data are shown as dots. The curve represents the expected yield based on the deuterium concentration.

for 50% He and bring into question whether the implosions are hydrodynamically equivalent. This would be consistent with an even greater degradation of the compression burn, reducing its importance compared to the shock burn and effectively elevating the average burn temperature.

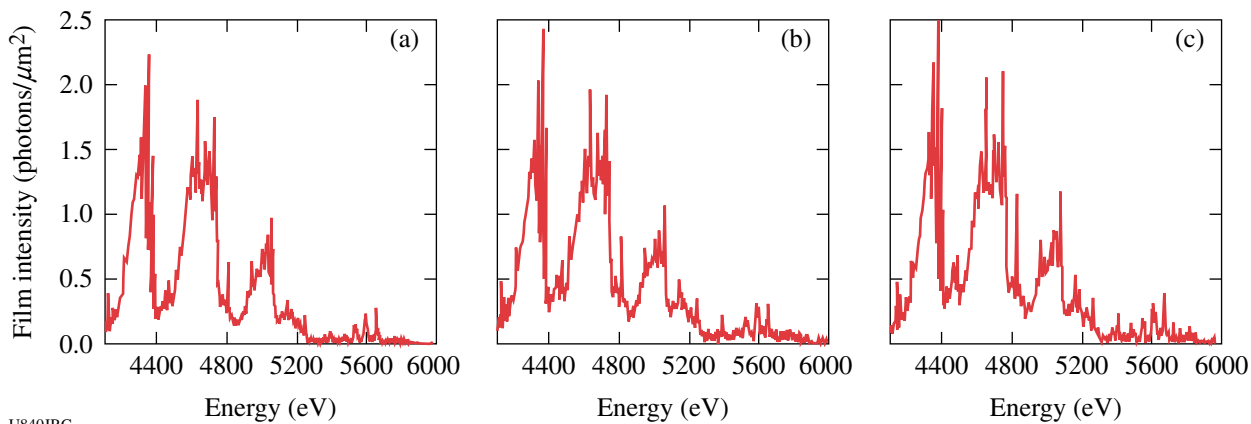
Overall, the results for doping the gas with ^3He were consistent with earlier results for Ar, Kr, and Xe, although a much larger atom fraction of ^3He was required to produce a similar effect.

NIF Platform #5: The NIF Platform #5 campaign continued experiments to develop diagnostic techniques for future NIF experiments. The FY08 experiments focused on backlighter source characterization and development as well as the successful execution of a new platform for the observation of absorption features due to heated materials.

One aspect of the backlighters that was examined was the conversion efficiency for L-shell and M-shell emitters. Over the course of the FY08 campaign, the studied laser irradiance varied from 10^{14} W/cm² up to nearly 10^{17} W/cm². The data obtained will assist in evaluating the expected photon fluxes at the NIF. An example of some of the data obtained from a CsI backlighter is shown in Fig. 116.96.

The platform for studying absorption spectroscopy is shown in Fig. 116.97. A Ti foil was heated inside a hohlraum. A CsI backlighter provided a quasi-continuum spectrum source, which passed through the sample and was recorded on by a spectrometer (Fig. 116.98). The recorded spectrum contains both the emission from the CsI backlighter and the absorption from the heated Ti foil. Although detailed analysis is still underway, these experiments provided valuable information on the absorption spectroscopy technique and have led to a number of improvements being implemented for future NIF experiments.

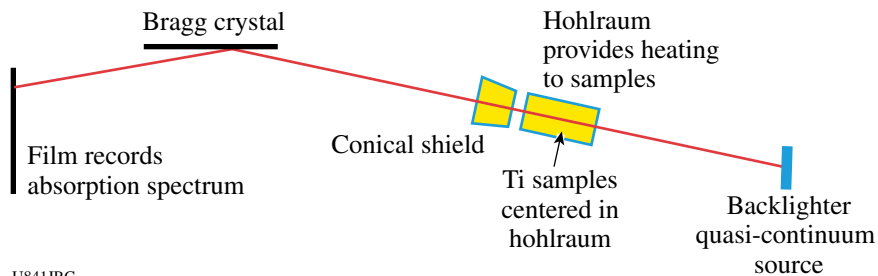
Synergy: We have used two cones of the OMEGA laser to irradiate a linear 0.7-scale NIF hohlraum to implode Be and CH capsules to measure the effect of beam phasing on the implosion symmetry. The vacuum hohlraums, with 2-mm-diam capsules, reached 105 eV using 1-ns laser pulses. The symmetry of the x-ray emission from the implosion was measured for both the CH and Be capsules. We were able to vary the symmetry at implosion time by varying the cone fraction or ratio of energy between the inner cones (21° or 42°) and the outer cone (59° beams) (Fig. 116.99). We found that the fraction where the best symmetry occurred was closest to those ratios that the re-emit



U840JRC

Figure 116.96

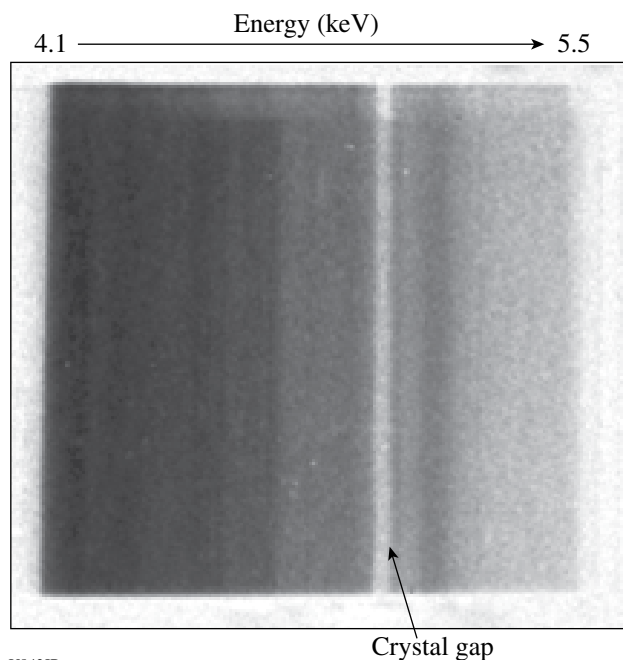
CsI spectra for (a) a nominal 600-, (b) nominal 400-, and (c) nominal 200- μm -diam spot. Note that although the laser irradiance spans an order of magnitude, the amount of emission stays essentially constant.



U841JRC

Figure 116.97

Schematic depicting the absorption spectroscopy configuration. Laser beams enter both sides of the hohlraum. A thin Ti foil sitting in the center of the hohlraum is then heated. The backlighter provides a quasi-continuum backlighter source, and its x rays pass through the Ti sample and are reflected off the Bragg crystal and recorded on film. Some of the backlighter emission is absorbed, depending on the temperature and density of the Ti. This schematic is not to scale.



U842JR

Figure 116.98

Spectrum containing the emission from a CsI backlighter and the absorption due to a thin, heated Ti foil.

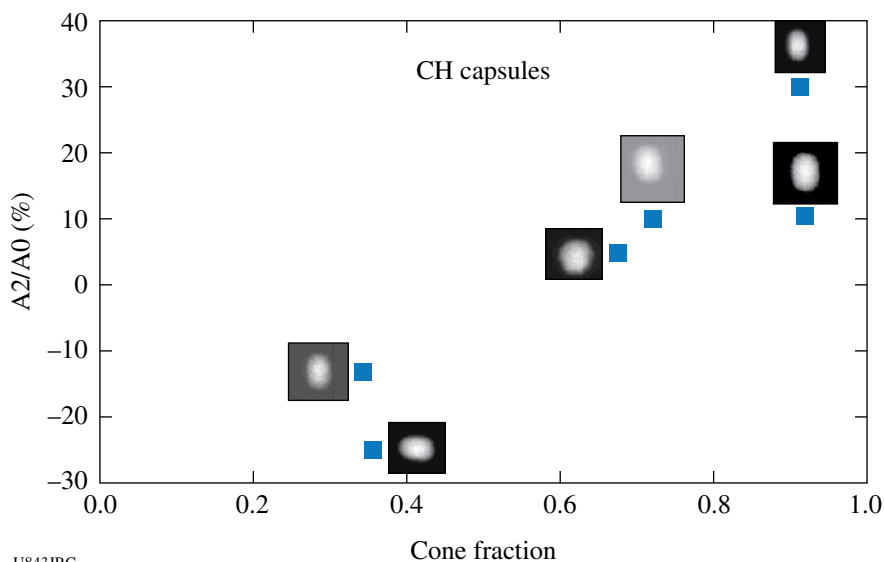


Figure 116.99
The measured second-order Legendre coefficient for the x-ray emission at the 30% level, measured at peak emission.

U843JRC

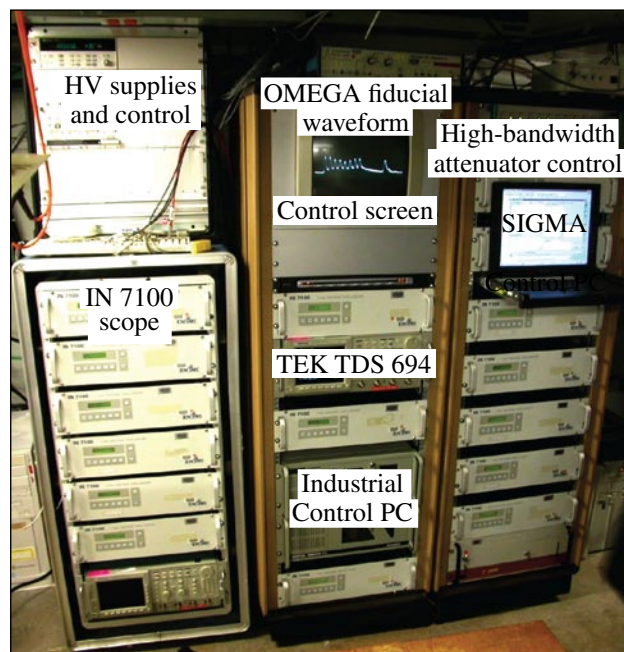
technique had found for the same pointing. When we replaced the 42° beams with the 21° beams and pointed to the same location in the hohlraum with the same laser irradiance, the hohlraum radiation was lower and the symmetry was affected, indicating some impaired propagation of the inner cone.

FY08 CEA OMEGA Experimental Programs

CEA conducted 39 target shots on the OMEGA Laser Facility in FY08. The CEA efforts included the following:

CEA Acquisition System and Software Developments for the OMEGA Facility: Since 1999 the development of specific CEA diagnostics for joint experiments with LLE, LANL, and LLNL on the OMEGA facility (for instance, DMX,²⁸ NIS,²⁹ or HRXI³⁰) have used the same devices (single-shot oscilloscopes, CCD, HV supply, switches, fast triggering generators, electrical attenuators, etc.) to supply and record detectors placed inside the target chamber area. All these recording and control devices are quite sensitive to the radiative environment generated during the OMEGA high-yield neutron shots ($Y_n > 10^{13}$ n/4π) induced mainly by the hard x-ray components for every shot or the neutron and gamma ray flux for high-neutron-yield shots.³¹ To protect these sensitive instruments, we decided to place them in a “quieter” radiative environment named “La Cave,” located in the basement of the target chamber area and protected by 70 cm of concrete. Figure 116.100 shows FPE (Force de Projection d’Enregistrement)—the recording system installed in La Cave that presently includes

- fourteen high-bandwidth single-shot oscilloscopes (IN 7100 – 7 GHz)



U852JRC

Figure 116.100
The CEA “FPE” acquisition system in the OMEGA “La Cave.”

- two digital oscilloscopes (TEKTRONIX TDS694 – 3 GHz)
- some HV supplies (used for biasing our detectors) and a related voltmeter
- a control system for our DMX high-bandwidth remotely controlled electrical attenuators

- a fast triggering system (not shown at the rear side of these cabinets)
- an automated control/command system

The CEA FPE control/command system, described in detail in the next paragraph, is based on PC hardware and is specially designed to automatically control our devices during the shot sequence when access to La Cave is closed for safety reasons. During that time (from 10 min prior to the shot to a few minutes after, depending on the radiative decay), each specific “order” generated during the OMEGA countdown process (during the capacitor bank charge), from a few minutes before until a few seconds after the shot, is recognized and used to automatically trigger some specific action on each device remotely controlled by the software (HV on, oscilloscope or CCD armed, data transfer and storage process, HV off, etc.). These actions can also be manually triggered by an operator if needed during the setup and preparation of the diagnostic. This system can be also be seen (for controlling its correct automated operation during the shot sequence) by the OMEGA experimental team operators when the relevant diagnostic is included as a “facility diagnostic” (as done, for example, for DMX).

“FPE-SIGMA” Command/Control System. Most of the deployment and tuning of the measurement chains of each CEA diagnostic is done by a “mobile” team (present at the OMEGA facility only during main CEA experiments) that uses a specific tool to manage the acquisition devices and their controlling network of computers.

Developed and improved over a decade, the “SIGMA” software tool solves computing issues going from manual to fully automated experiments. A distributed architecture—which also downsizes to fit into a single computer—is controlled at one place by human interface. The tool supports the diagnostic design and improvement process by making it possible to describe the system in a smart graphical interface (the Microsoft Visio diagram editor is shown in Fig. 116.101). The targets, filters, and mirrors (the main components of DMX) appear at the left side of a schematic view in which the signal paths and delays also appear and can be documented. Thus the settings definition of each remote-controllable device is postponed after the definition of its use case. In fact, in an automated diagnostic, settings are sets of logical data that are selectively recalled into a static physical layer. The versatility of a physical layer increases with the remote controllability of its key components.

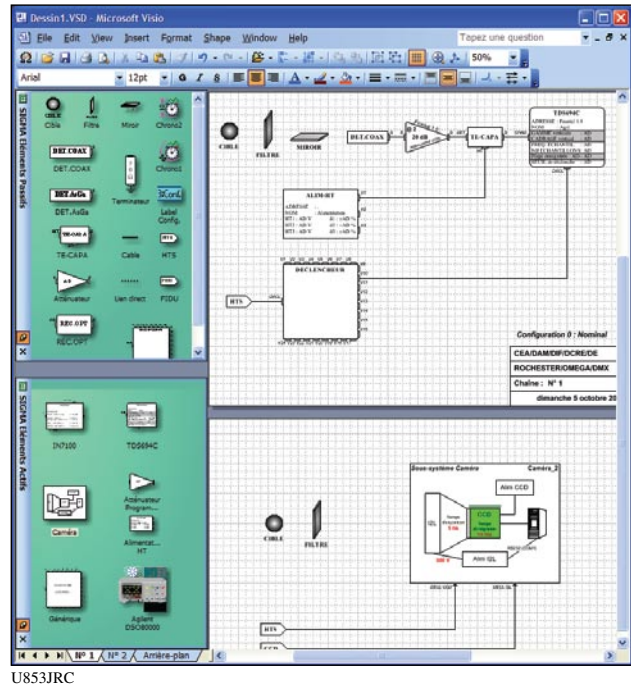


Figure 116.101
The diagnostic editor built over Microsoft Visio.

The underlying and hidden computing technologies include

- specific support of a few device drivers (GPIB controller, ISA/PCI imaging cards, USB devices)
- standard communication with serial ports, GPIB ports, TCP/IP connections, and ODBC databases

In addition, the complexity of some instrumental subsystems—e.g., based on more than one device connected to different ports, leading to advanced communication handshake or to advanced commands implementation—was hidden in high-level virtual device drivers that run on the device computers and expose a GPIB-like interface.

The supported classes of instruments come with a visual schematic footprint, an inline OCX front panel, a guarded OCX settings form, and a set of intrinsic commands provided by design. Intrinsic commands may generate specific event types that also come with their suite of *in-situ* viewers and commands.

Currently, the SIGMA software controls analog and digital oscilloscopes, power supplies, programmable attenuator banks, and neutronic imaging subsystems. At design time, the Visio multipage editor is fully automated to show the instrument settings according to the active configuration. At run time, the

configuration variable is also maintained and its value can be automatically affected in order to influence the conduct of operations. For example, the active configuration can be retrieved from a database each time a shot number is received.

Ten configurations are currently supported, each being freely labeled. At the instrument level, four sets of settings are freely associated to the ten configurations. Settings factorization across configurations simplifies diagnostic management. At the diagnostic level, a matrix determines the physical subsets (measurement chain) that are active with each configuration.

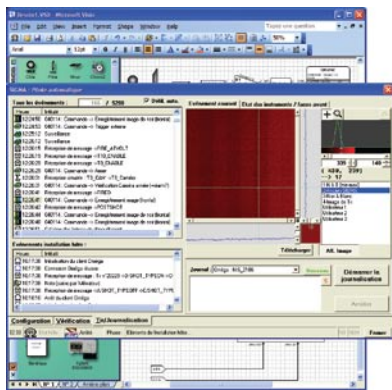
An experiment can be controlled manually, in a semi-automatic manner (triggering scripted sequences), or fully automatic [involving the internal scheduler or listening to a hierarchical uplink (supervisor)]. Supervisors can also be notified when selected error levels occur.

During a run time, the software builds a single chronology of time-stamped and typed events. Each event type shows a specific icon and comes with a set of tools that makes possible

inspection (texts, forms, curves, or pictures), event navigation, or procedure recall. Past-event inspection is possible at any time, as well as single command executions, script executions, and inspection/modification of instrument settings. The guarded variables cover every aspect of the system except the state of the user interface.

Recently, the SIGMA tool was qualified to be integrated into the OMEGA operations as the DMX diagnostic application controller. To make the startup and the stopdown of the diagnostic application easier, the tool was given a simplified alternate interface showing a strictly filtered set of notifications (Fig. 116.102). In addition, the non-specialist is guided from the first power up to the last shutdown thanks to a localized operator sheet (Fig. 116.103) and to the firing of some interactive checklists. In the meantime, the software monitors the presence of each component.

The SIGMA software developed and tested initially for OMEGA common experiments is also deployed at the LULI facility (Palaiseau, France) and the LIL facility (Cesta, France); CEA



U854JRC

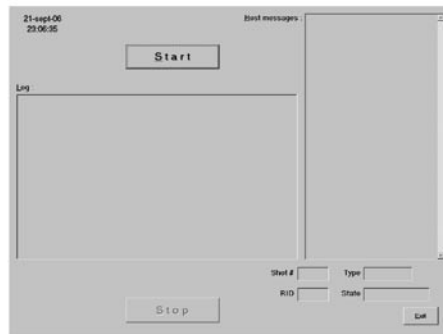
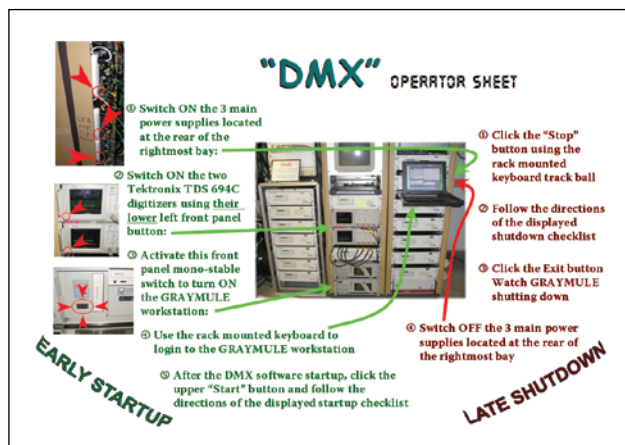


Figure 116.102
The complete versus the simplified run-time human interface.



U855JRC

Figure 116.103
An operator sheet to properly start the minimum hardware and launch the checklist.

also uses it on its Gekko XII diagnostic (Osaka, Japan), justifying its given name of FPE for “Projected Force for Recording.”

Monocrystalline CVD Diamond Detector: A Novel Tool for Neutron Yield and Duration Emission Measurement: Synthetic diamond detectors are now known to exhibit attractive characteristics to discriminate neutrons by the time-of-flight technique (nTOF), as well as to measure neutron bang time and ion temperature. Earlier work had, however, demonstrated how the quality of this material matters since the temporal properties of synthetic diamond devices (aiming to be in the 100-ps range) strongly differ from device to device and growth origins. For the record, sensitive CVD diamonds are usually too slow to be used for timing measurement, although such a development of sensitive and fast CVD diamonds would make it possible to perform simultaneously both neutron-yield and ion-temperature measurements, thus minimizing the number of nTOF detectors on the Laser Megajoule Facility.

More recently, and to complete the data acquired in 2007 (Ref. 32) for low-neutron-yield measurements, a new series of polycrystalline CVD diamonds (Element Six) and new monocrystalline CVD diamonds (CEA-LIST, Saclay) were implemented on the OMEGA Laser Facility during implosion experiments of DT capsules yielding 10^{13} to 10^{14} neutrons. These materials exhibited higher sensitivities. The goal was to determine how such novel materials could be relevant for neutron-yield, bang-time, and ion-temperature diagnostics.

On OMEGA, diamond detectors were inserted at distances of 30 cm, 1 m, and 2 m from the target chamber center using the TIM diagnostic insertion mechanisms. Other diamonds were placed outside the target chamber at 3.3 m from target chamber center (TCC). Distances and neutron-yield ranges provide the ability to probe the detectors' performances within two decades of the neutron flux (n/cm^2). The detectors exhibit a linear response over the dynamic range explored. To compare diamond materials, their sensitivities were normalized as a

function of the sample volume: diamond sensitivity can often vary by several orders of magnitude, up to three decades previously observed. Table 116.V shows that the novel monocrystalline sample A260107B (from CEA-LIST) appears to be the most sensitive of all diamond material calibrated on OMEGA from the campaigns in 2007 and 2008.

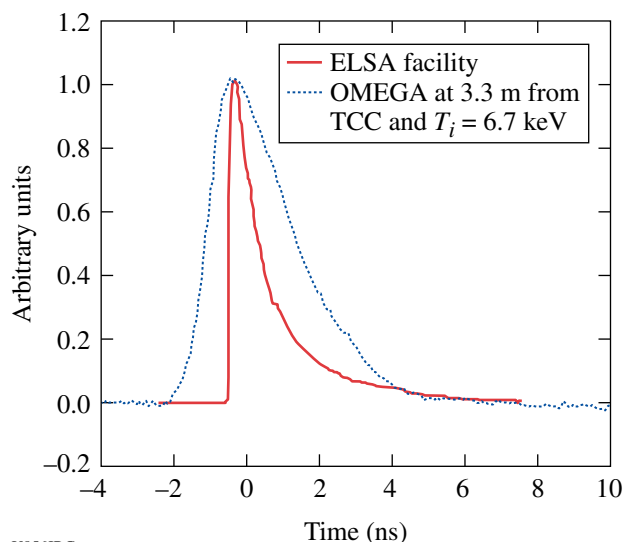
Prior to the experiments, we had evaluated the temporal properties of these diamonds under 16-MeV electrons produced on a Linac accelerator at CEA (ELSA at Bruyères-le-Châtel). The pulse duration on ELSA is about 25 ps, making it possible to measure the main timing parameters. The monocrystalline diamond A260107B pulse shape has a 10% to 90% rise time that remains below 100 ps. Such temporal properties make this sensitive diamond a good candidate to measure the Doppler broadening of the neutron pulse along its propagation, thus enabling one to measure the ion temperature at bang time.

On OMEGA, the detector signal must propagate through 10 to 30 m of cable before it reaches the 7-GHz-bandwidth single-shot oscilloscope (IN7100). We have developed a software processing tool that makes it possible to deconvolve the pulse broadening produced by such a high cable length. It led to processed signals exhibiting rise times of 870 ps at 3.3 m from TCC with an ion temperature of 6.7 keV (Fig. 116.104). This signal rise time observed during DT implosions results from the 150-ps burn duration, convoluted with the temporal broadening induced by the DT ion's main energy at bang time.

Using the signal-processing technique already used in NTD diagnostics,³³ we can deduce the neutron pulse duration at 3.3 m from the target, which is mainly determined by the Doppler broadening produced by the ions. The resulting ion temperature and measured time duration are shown in the two last columns of Table 116.VI. The inferred ion temperatures from the CVD diamond signal are in good agreement with the standard OMEGA measurement performed at 5 m with a fast scintillator and an MCP photomultiplier and are presented for

Table 116.V: Diamond sensitivity measured under 14-MeV neutrons pulses.

CVD	Type	Thickness	Size	Gold Contact	High Voltage	Sensitivity (C/n/cm ³)
A260107B	Monocrystalline	500 μ m	4 \times 4 mm	3 \times 3 mm	-1400 V	3.1×10^{-15}
A281103	Polycrystalline	260 μ m	5 \times 5 mm	4 \times 4 mm	-360 V	1.8×10^{-15}
E6 300 μ m	Polycrystalline	300 μ m	ϕ 10 mm	ϕ 8 mm	-750 V	2.4×10^{-16}
E6 1 mm	Polycrystalline	1000 μ m	ϕ 10 mm	ϕ 8 mm	-1000 V	1.3×10^{-16}
A270105	Polycrystalline	115 μ m	5 \times 5 mm	4 \times 4 mm	-750 V	4.7×10^{-17}
A190106	Polycrystalline	450 μ m	5 \times 5 mm	4 \times 4 mm	-500 V	4.9×10^{-18}



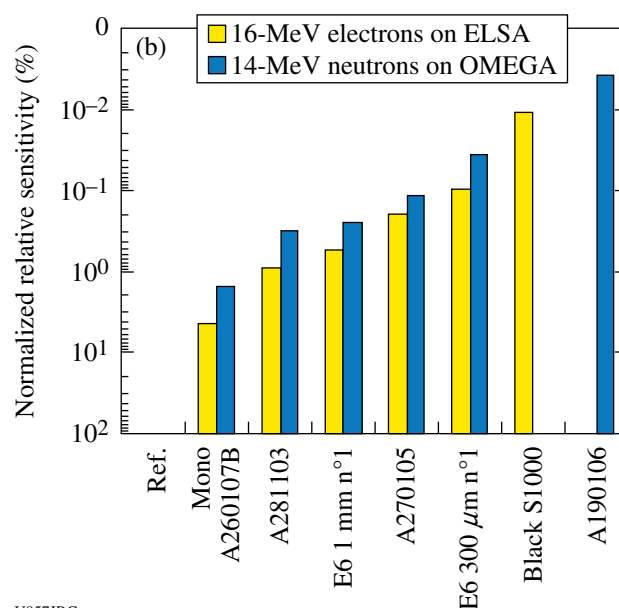
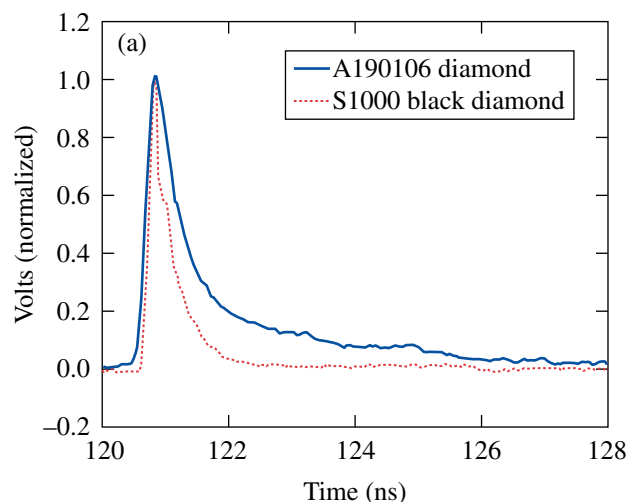
U856JRC

Figure 116.104

Comparison of a monocrystalline pulse shape measured on ELSA (solid curve) and OMEGA (dotted curve).

comparison in Table 116.VI. As predicted, monocrystalline CVD diamonds made by CEA-LIST (A260107B) are sensitive enough for neutron-yield measurements and fast enough for ion-temperature measurements.

Low-sensitivity diamonds are also required for neutron high-yield measurements. A polycrystalline diamond (A190106 from CEA-LIST) grown using a high level of nitrogen impurity was tested on OMEGA; it exhibited a very low sensitivity but also a very long pulse tail. A “black diamond” detector (from Applied Diamond) exhibiting high levels of “non-carbon impurities” was provided by V. Yu. Glebov of LLE. These two diamond samples were evaluated at the ELSA facility using 16-MeV electrons to compare their relative sensitivities and timing parameters (Fig. 116.105). Comparison with other diamonds tested on ELSA and OMEGA shows that those black diamonds are probably good “low-sensitivity” detectors for high neutron-yield measurements on MJ-class lasers.



U857JRC

Figure 116.105

Comparison of pulse shape and electron–neutron relative sensitivity. Relative sensitivities are normalized to earlier measurements on one of the most-sensitive diamonds.

Table 116.VI: Ion-temperature measurement with monocrystalline CVD diamond at 3.3 m from TCC.

OMEGA Measurement			CVD Diamond Measurement		
Shot	Ti LLE (± 0.5 KeV)	Δt	CVD reference	Ti measured	Δt measured
51301	6.4 keV	992 ps	A260107B	6.7 keV	1016 ps
51305	5.3 keV	903 ps	A260107B	5.2 keV	893 ps
51314	3.6 keV	744 ps	A260107B	3.7keV	729 ps
51315	3.7 keV	754 ps	A260107B	3.6 keV	740 ps
51322	5.5 keV	919 ps	A260107B	5.6 keV	926 ps
51325	5.1 keV	885 ps	A260107B	5.1 keV	882 ps

The 2008 campaigns have therefore enabled us to identify families of materials that appear suitable according to measurement objectives. This development of faster high- and low-sensitivity CVD diamond detectors is still being investigated with CEA-LIST and LLE. A new challenge will now be to demonstrate that a large, sensitive CVD diamond is capable of measuring the downscattered neutron yield for ρR determination.

Neutron Imaging on OMEGA: For several years, CEA has obtained neutron-imaging measurements on OMEGA with an overall resolution of $20\ \mu\text{m}$ (Refs. 29 and 34). The imaging system is based on a small aperture (a 2-mm-diam hole made in a 10-cm-thick tungsten cylinder) placed 260 mm from TCC.³⁵ The detector (80-mm diameter) is then set 8 m from the target. In this setup, aligning the aperture is very difficult due to the fact that any small misalignment entails a large displacement of the target image on the detector plane at 8 m. As shown with the penumbral aperture last year, there is also the influence of the source position inside the field of view, which is $200\ \mu\text{m}$ for a source size of approximately $50\text{-}\mu\text{m}$ FWHM.^{35,36}

In FY07 we presented the effects of misalignment on both calculated and experimental unfolded images obtained with a penumbral aperture. Distortions entailed on the image shape revealed that aperture-positioning tolerance is about $50\ \mu\text{m}$ within the field of view to prevent any effects from misalignment on unfolded images. Briefly, our alignment technique uses a telescope and a beam splitter to view the target through the aperture and the detector, thus fixing the detector–target axis. Next, the aperture is aligned using picomotors on this axis. This technique is very accurate but quite long and fastidious. To meet OMEGA repetition rate and shot plan requirements, a new technique for coarse alignment was tested this year to earn time for setting up before shots. For fine alignment, the old technique is then performed. The new technique relies on a laser beam being injected inside the TIM by a single-mode optical fiber. The laser is sent in two collinear directions via a semitransparent plate, one through the aperture and one to the detector. The first allows us to be sure that we are well centered both on the target and the aperture, the second on the detector. Such a system permits us to be ready for a shot in about 1 h, compared to approximately 2.5 h in the past. We have thus obtained a usable image well centered on the detector on the first shot (51295, see Fig. 116.106).

For high SNR images, we use an annular aperture (see Fig. 116.107) to form neutron images.³⁴ This aperture is made with a biconical plug inserted in the penumbral aperture, but,

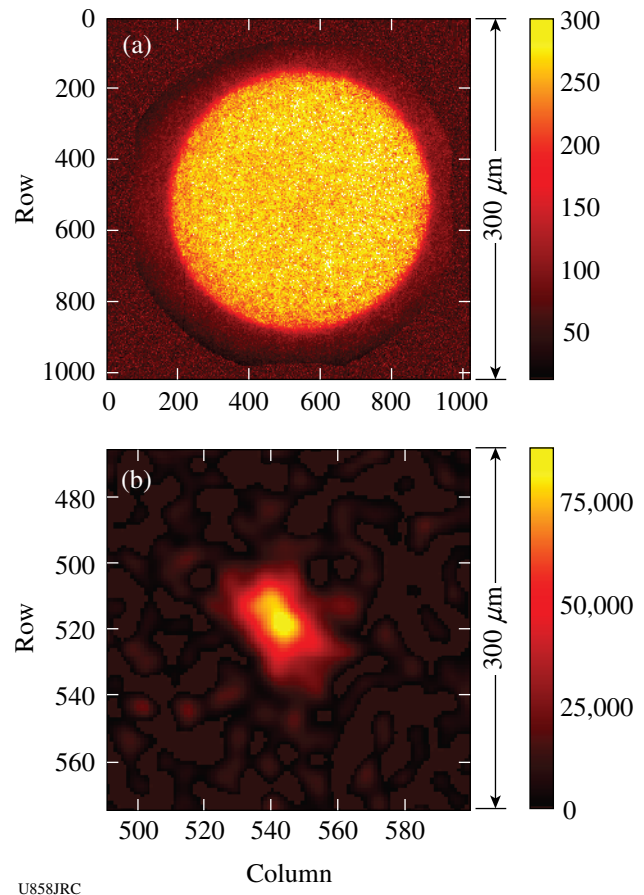
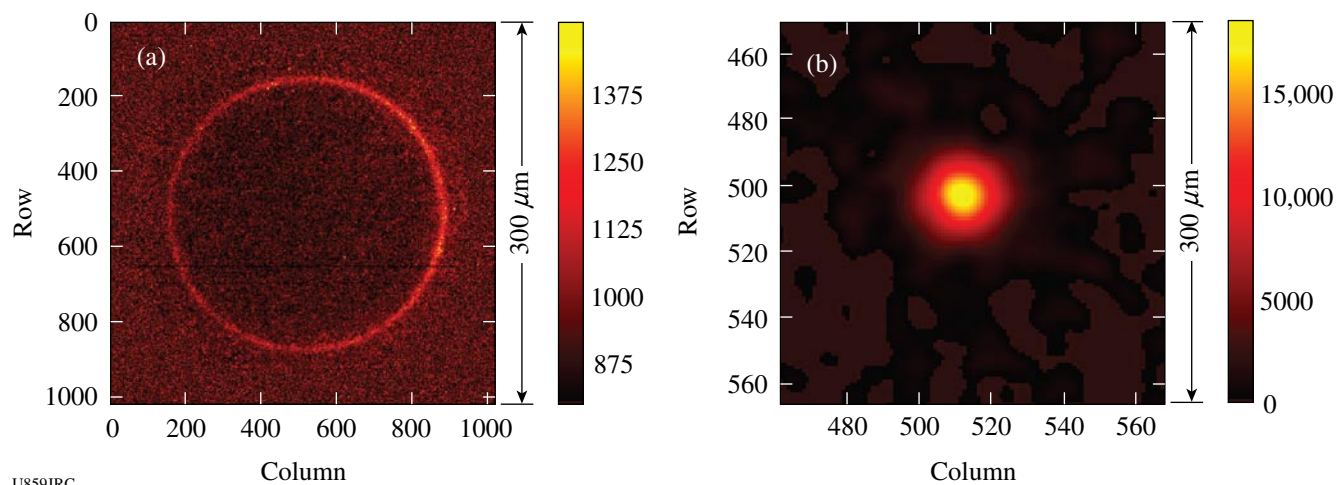


Figure 116.106

Image of DT implosion (shot 51295) yielding 4.0×10^{12} neutrons. (a) Raw image and (b) unfolded image using autocorrelation method³⁷ (SNR = 17).

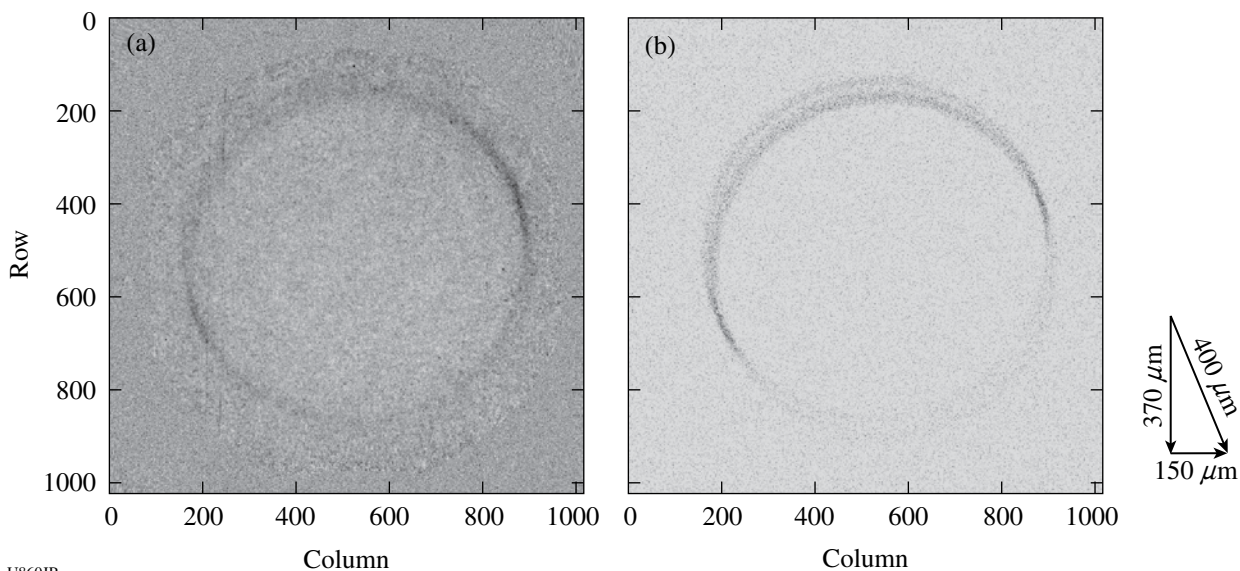
in this case, there is no opportunity to send the laser through the aperture. Alignment precision then relies on the capability of reproducing two identical penumbral apertures that can be replaced with minimal misalignment. Aperture positioning tolerance and repeatability between these two apertures were quantified in our laboratory and verified during several campaigns on OMEGA. As for the penumbral aperture, this year (FY08) we studied image distortion as varying annular aperture alignment on OMEGA experiments. These results were compared to Monte Carlo calculations (Geant4)³⁸ and showed relatively good agreement with experimental results (see Fig. 116.108).

The oblate shape of Fig. 116.106(b) reveals that the aperture is not perfectly aligned; this image was $\sim 200\ \mu\text{m}$ off center. This misalignment was due to the TIM insertion/reinsertion cycle before the shot for adding tritium protection. Alignment control is impossible after tritium coverage addition. It was found that feedback springs on picomotors were not strong



U859JRC

Figure 116.107
 (a) Raw image of DT implosion (shot 51324) yielding 2.8×10^{13} neutrons. (b) Unfolded image using autocorrelation method³⁷ (SNR = 41).



U860JR

Figure 116.108
 (a) Image of DT implosion (shot 51304) yielding 3.2×10^{13} neutrons. (b) Calculated image using Geant4 with 50- μ m-diam neutron source off center by 400 μ m (150 μ m right and 370 μ m down).

enough to recover the right position during insertion vibrations. Alignment technique was not responsible for this error.

The capability of being well aligned on a first shot is a crucial point for megajoule-class lasers with a 40-m line of sight. Misalignment contributors are now well known and can be reduced under acceptable values less than 50 μ m. We are currently qualifying a 150-mm-diam camera for high-resolution measurements (down to 10 μ m) that next year will be placed at 13 m from target.

FY08 AWE OMEGA Experimental Programs

Thirty-two target shots were taken for AWE-led experiments on OMEGA in FY08. Hohlräum symmetry was one of the principal topics of investigation.

Coupling laser energy into a hohlraum is a long-established method for generating a symmetric x-ray drive for high-convergence implosions. A number of studies of hohlraum symmetry have been undertaken to optimize the conditions for inertial confinement fusion,^{39,40} therefore our codes are

relatively well validated in this regime. In certain situations, it is necessary to perturb the symmetry of the driver, for example, where beams are required for diagnostic purposes. To validate our simulations in such conditions, AWE has commenced a campaign to study the energetics of asymmetric hohlraums.

A laser-heated hohlraum was used (Fig. 116.109) and driven either from both ends ("symmetric drive") or from only one end ("asymmetric drive"). The OMEGA Dante diagnostic is used to measure temporal evolution of the radiation temperature. A capsule located at the center of the hohlraum is used as a diagnostic of the flux uniformity radiographed with a titanium area backlighter. Two classes of capsules with a nominal diameter of $600\ \mu\text{m}$ were fielded on the first shot day (September 2008). A silicon aerogel sphere ($\rho \sim 325\ \text{mg/cc}$) makes it possible to characterize the time-dependent drive as a function of angle via the steep x-ray transmission gradient just outside the converging ablation front. A plastic-coated, thin-shelled glass capsule provides a complementary measure of the angular variation in absorbed flux. The outer plastic layer serves to mitigate the backlighter attenuation from the ablated material, while the

glass shell provides an opaque tracer layer for the radiography. For some targets a thin gold layer was applied over the diagnostic holes to maximize the albedo and reduce any azimuthal variation in the dynamics.

Figure 116.110 illustrates the late-time implosion dynamics of a thin-shell glass capsule driven from one side and synthetic radiographs produced from AWE's *NYM* radiation hydrocode. The experimental data indicate that the ablation is preferentially directed toward the laser spots, with a slightly reduced drive on axis adjacent to the laser entrance hole. This results in an inwardly propagating shock that converges on axis, driving a collimated jet ahead of the main shock front. The preliminary calculations of these targets qualitatively reproduce the macroscopic evolution of the implosion but overestimate the velocity of the shell. The radiographic images of the aerogel spheres show a clear departure from sphericity (Fig. 116.111). Contours of the backlighter transmission, coupled with the original location of the sphere, make a Legendre polynomial fit to the data possible. This indicates a significant P_1 mode resulting from the imposed drive imbalance within the hohlraum.

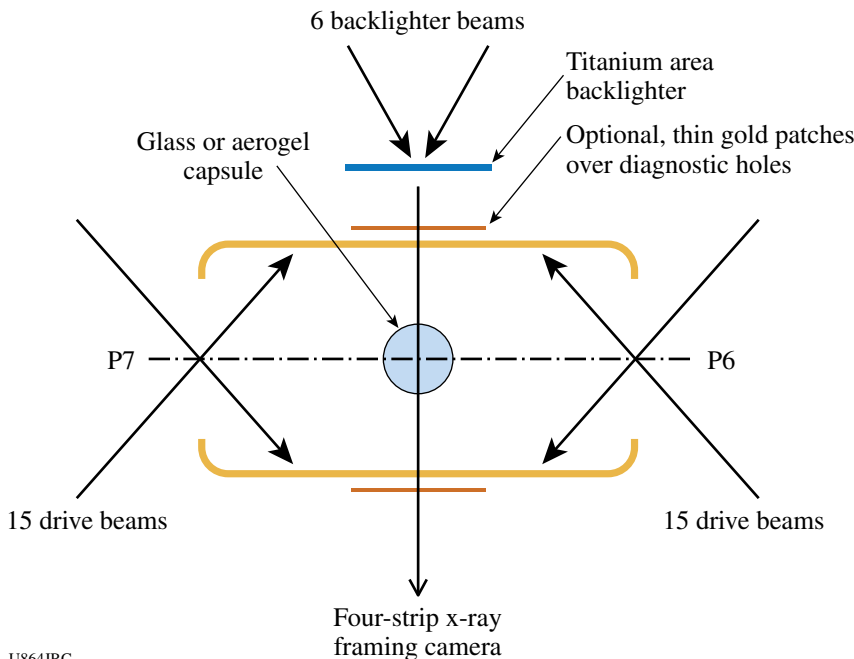


Figure 116.109
Schematic of the experiment to investigate the performance of an asymmetrically driven hohlraum. The $600\text{-}\mu\text{m}$ -diam spherical capsule is placed at the center of a 1.6-mm -diam hohlraum target that is heated through both laser entrance holes (symmetric-drive case) or through just one laser entrance hole (asymmetric-drive case). Radiographic measurements of the implosion are made using a titanium area backlighter and a four-strip x-ray framing camera.

U864JRC

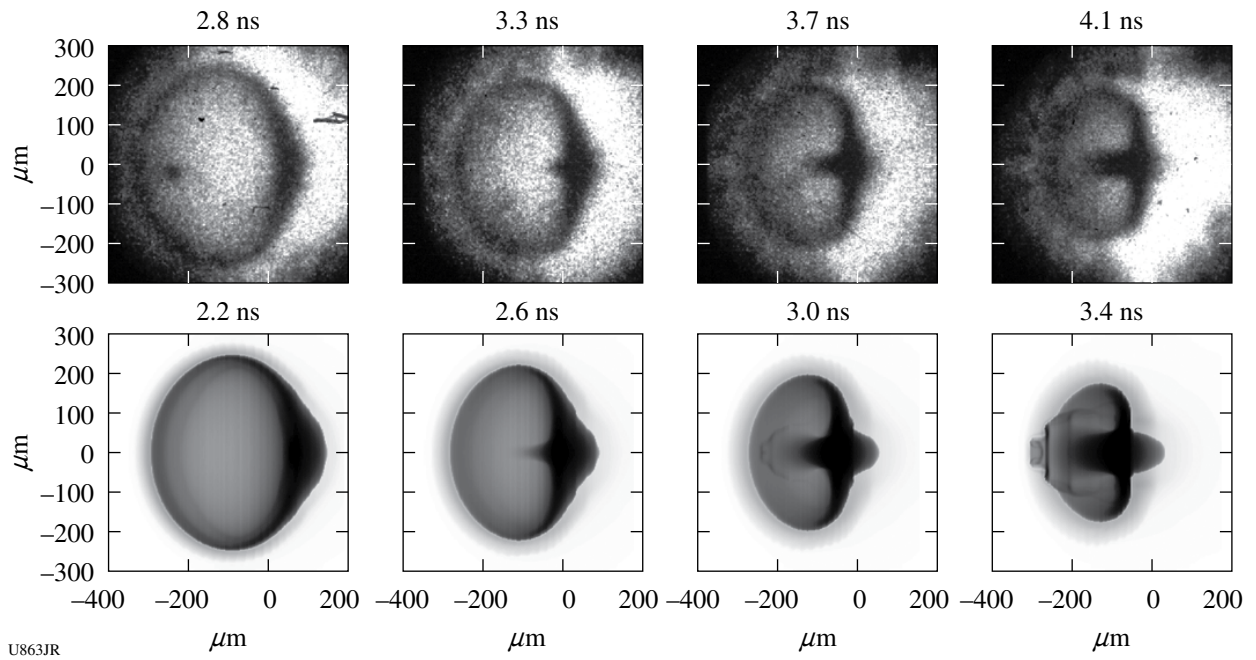


Figure 116.110 Radiographs of the capsule implosion (top) compared with synthetic radiographs (bottom) obtained by post-processing simulations using the AWE 2-D radiation hydrodynamics code *NYM*.

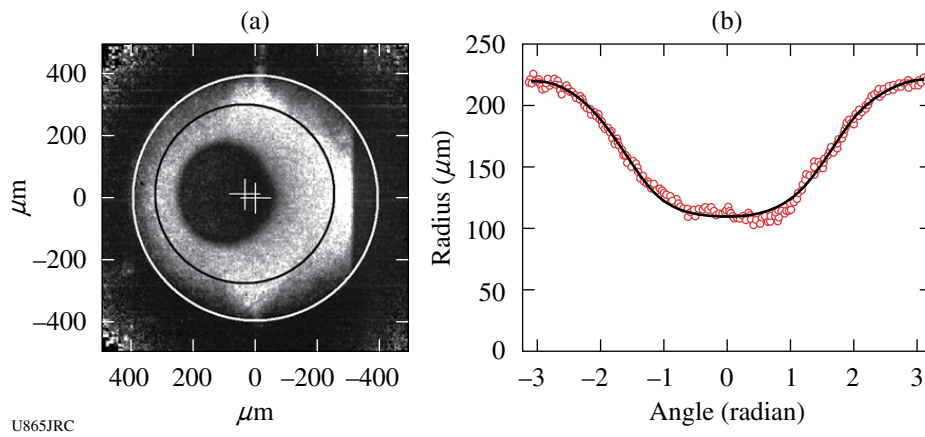


Figure 116.111 (a) Radiograph of an asymmetrically driven silica-aerogel sphere at 2.5 ns after onset of the radiation drive. The superimposed circles represent the initial positions of the aerogel sphere and diagnostic hole (the sphere and hole centers are shown by the crosses), and (b) Legendre-polynomial fit to the contour of transmitted backlighter intensity = 0.4. The inferred values of the first four Legendre coefficients are 156 μm (P_0), 62 μm (P_1), 4.3 μm (P_2), and 7.3 μm (P_3).

REFERENCES

1. C. K. Li, F. H. Séguin, J. A. Frenje, J. R. Rygg, R. D. Petrasso, R. P. J. Town, P. A. Amendt, S. P. Hatchett, O. L. Landen, A. J. Mackinnon, P. K. Patel, V. A. Smalyuk, T. C. Sangster, and J. P. Knauer, *Phys. Rev. Lett.* **97**, 135003 (2006).
2. C. K. Li, F. H. Séguin, J. A. Frenje, J. R. Rygg, R. D. Petrasso, R. P. J. Town, P. A. Amendt, S. P. Hatchett, O. L. Landen, A. J. Mackinnon, P. K. Patel, M. Tabak, J. P. Knauer, T. C. Sangster, and V. A. Smalyuk, *Phys. Rev. Lett.* **99**, 015001 (2007).
3. C. K. Li, F. H. Séguin, J. A. Frenje, J. R. Rygg, R. D. Petrasso, R. P. J. Town, O. L. Landen, J. P. Knauer, and V. A. Smalyuk, *Phys. Rev. Lett.* **99**, 055001 (2007).
4. C. K. Li, F. H. Séguin, J. R. Rygg, J. A. Frenje, M. Manuel, R. D. Petrasso, R. Betti, J. Delettrez, J. P. Knauer, F. Marshall, D. D. Meyerhofer, D. Shvarts, V. A. Smalyuk, C. Stoeckl, O. L. Landen, R. P. J. Town, C. A. Back, and J. D. Kilkenny, *Phys. Rev. Lett.* **100**, 225001 (2008).
5. J. R. Rygg, F. H. Séguin, C. K. Li, J. A. Frenje, M. J.-E. Manuel, R. D. Petrasso, R. Betti, J. A. Delettrez, O. V. Gotchev, J. P. Knauer, D. D. Meyerhofer, F. J. Marshall, C. Stoeckl, and W. Theobald, *Science* **319**, 1223 (2008).
6. C. K. Li, F. H. Séguin, J. A. Frenje, J. R. Rygg, R. D. Petrasso, R. P. J. Town, P. A. Amendt, S. P. Hatchett, O. L. Landen, A. J. Mackinnon, P. K. Patel, V. Smalyuk, J. P. Knauer, T. C. Sangster, and C. Stoeckl, *Rev. Sci. Instrum.* **77**, 10E725 (2006).
7. C. K. Li, F. H. Séguin, J. A. Frenje, M. Manuel, R. D. Petrasso, V. A. Smalyuk, R. Betti, J. Delettrez, J. P. Knauer, F. Marshall, D. D. Meyerhofer, D. Shvarts, C. Stoeckl, W. Theobald, J. R. Rygg, O. L. Landen, R. P. J. Town, P. A. Amendt, C. A. Back, and J. D. Kilkenny, *Plasma Phys. Control. Fusion* **51**, 014003 (2009).
8. R. Petrasso, *Bull. Am. Phys. Soc.* **52**, 97 (2007).
9. C. K. Li, *Bull. Am. Phys. Soc.* **53**, 20 (2008).
10. C. K. Li, F. H. Séguin, J. A. Frenje, J. R. Rygg, R. D. Petrasso, R. P. J. Town, P. A. Amendt, S. P. Hatchett, O. L. Landen, A. J. Mackinnon, P. K. Patel, V. Smalyuk, J. P. Knauer, T. C. Sangster, and C. Stoeckl, *Rev. Sci. Instrum.* **77**, 10E725 (2006).
11. S. H. Glenzer *et al.*, *Phys. Rev. Lett.* **90**, 175002 (2003).
12. J. J. MacFarlane, I. E. Golovkin, and P. R. Woodruff, *J. Quant. Spectrosc. Radiat. Transf.* **99**, 381 (2006).
13. H. J. Lee *et al.*, "X-Ray Thomson Scattering Measurements of Density and Temperature in Shock-Compressed Beryllium," to be published in *Physical Review Letters*.
14. D. H. Froula *et al.*, *Phys. Rev. Lett.* **101**, 115002 (2008); D. H. Froula *et al.*, *Phys. Rev. Lett.* **100**, 015002 (2008).
15. P. Neumayer *et al.*, *Phys. Rev. Lett.* **100**, 105001 (2008); P. Neumayer *et al.*, *Phys. Plasmas* **15**, 056307 (2008).
16. E. L. Dewald *et al.*, *Rev. Sci. Instrum.* **79**, 10E903 (2008).
17. R. K. Kirkwood *et al.*, *Phys. Plasmas* **16**, 012702 (2009).
18. H.-S. Park *et al.*, "Experimental Tests of Vanadium Strength Models at High Pressures and High Strain Rates," *International Journal of Plasticity* (in preparation).
19. B. A. Remington *et al.*, "A Path to Materials Science at Extreme Pressures," *International Journal of Plasticity* (in preparation).
20. S. Prisbrey *et al.*, "3-D Hohlraum Simulations for an Indirect-Drive Strength Platform," *International Journal of Plasticity* (in preparation).
21. S. Pollaine *et al.*, "Thin Walled Hohlraum Designs for High Pressure, Stagnation Free Loading," *International Journal of Plasticity* (in preparation).
22. A. B. Reighard *et al.*, *Rev. Sci. Instrum.* **79**, 10E915 (2008).
23. K. B. Fournier *et al.*, "Absolute X-Ray Yields from Laser-Irradiated Ge-Doped Low-Density Aerogels," *Physics of Plasmas* (in preparation).
24. J. F. Hansen *et al.*, *Rev. Sci. Instrum.* **79**, 013504 (2008).
25. P. E. Young *et al.*, *Phys. Rev. Lett.* **101**, 035001 (2008).
26. J. R. Rygg, J. A. Frenje, C. K. Li, F. H. Séguin, R. D. Petrasso, J. A. Delettrez, V. Yu. Glebov, V. N. Goncharov, D. D. Meyerhofer, S. P. Regan, T. C. Sangster, and C. Stoeckl, *Phys. Plasmas* **13**, 052702 (2006).
27. D. C. Wilson, G. A. Kyrala, J. F. Benage Jr., F. J. Wysocki, M. A. Gunderson, W. J. Garbett, V. Yu. Glebov, J. Frenje, B. Yaakobi, H. W. Herrman, J. H. Cooley, L. Welser-Sherrill, C. J. Horsfield, and S. A. Roberts, *J. Phys., Conf. Ser.* **112**, 022015 (2008).
28. J. L. Bourgade *et al.*, *Rev. Sci. Instrum.* **72**, 1173 (2001).
29. L. Disdier, A. Rouyer, A. Fedotoff, J.-L. Bourgade, F. J. Marshall, V. Yu. Glebov, and C. Stoeckl, *Rev. Sci. Instrum.* **74**, 1832 (2003).
30. J. L. Bourgade, P. Troussel, A. Casner, G. Huser, T. C. Sangster, G. Pien, F. J. Marshall, J. Fariaud, C. Redmond, D. Gontier, C. Chollet, C. Zuber, C. Reverdin, A. Richard, P. A. Jaanimagi, R. L. Keck, R. E. Bahr, W. J. Armstrong, J. Dewandel, R. Maroni, F. Aubard, B. Angelier, C. Y. Cote, and S. Magnan, *Rev. Sci. Instrum.* **79**, 10E904 (2008).
31. J. L. Bourgade, V. Allouche, J. Baggio, C. Bayer, F. Bonneau, C. Chollet, S. Darbon, L. Disdier, D. Gontier, M. Houry, H. P. Jacquet, J.-P. Jadaud, J. L. Leray, I. Masclet-Gobin, J. P. Negre, J. Raimbourg, B. Villette, I. Bertron, J. M. Chevalier, J. M. Favier, J. Gazave, J. C. Gomme, F. Malaise, J. P. Seaux, V. Yu. Glebov, P. Jaanimagi, C. Stoeckl, T. C. Sangster, G. Pien, R. A. Lerche, and E. Hodgson, *Rev. Sci. Instrum.* **75**, 4204 (2004).
32. *LLE Review Quarterly Report* **112**, 203, Laboratory for Laser Energetics, University of Rochester, Rochester, NY, LLE Document No. DOE/SF/19460-790 (2007).
33. R. A. Lerche, D. W. Phillion, and G. L. Tietbohl, *Rev. Sci. Instrum.* **66**, 933 (1995).

34. L. Disdier, A. Rouyer, I. Lantuéjoul, O. Landoas, J. L. Bourgade, T. C. Sangster, V. Yu. Glebov, and R. A. Lerche, *Phys. Plasmas* **13**, 056317 (2006).
35. *LLE Review Quarterly Report* **112**, 270, Laboratory for Laser Energetics, University of Rochester, Rochester, NY, LLE Document No. DOE/SF/19460-790 (2007).
36. M. C. Ghilea, T. C. Sangster, D. D. Meyerhofer, R. A. Lerche, and L. Disdier, *Rev. Sci. Instrum.* **79**, 023501 (2008).
37. A. Rouyer, *Rev. Sci. Instrum.* **74**, 1234 (2003).
38. S. Agostinelli, *et al.*, *Nucl. Instrum. Methods Phys. Res. A* **506**, 250 (2003); <http://geant4.web.cern.ch/geant4>.
39. S. G. Glendinning, P. Amendt, B. D. Kline, R. B. Ehrlich, B. A. Hammel, D. H. Kalantar, O. L. Landen, R. E. Turner, R. J. Wallace, T. J. Weiland, N. Dague, J.-P. Jadaud, D. K. Bradley, G. Pien, and S. Morse, *Rev. Sci. Instrum.* **70**, 536 (1999).
40. S. M. Pollaine *et al.*, *Phys. Plasmas* **8**, 2357 (2001).

